Cement and Concrete Composites 144 (2023) 105268

Contents lists available at ScienceDirect

Cement and Concrete Composites

journal homepage: www.elsevier.com/locate/cemconcomp

Hydration and phase evolution of blended cement composites containing lithium and saturated metakaolin

Dayou Luo, Jianqiang Wei *

Department of Civil and Environmental Engineering, Francis College of Engineering, University of Massachusetts Lowell, Lowell, MA, 01854, USA

ARTICLE INFO

Keywords:
Cement composites
Metakaolin
Hydration
Phase evolution
D. Chemical analysis

ABSTRACT

Although the high efficiency of coupled lithium and saturated metakaolin in alkali-silica reaction mitigation has been documented, its influence on cement hydration remains uninvestigated. In this study, saturated metakaolin with varying degrees of saturation and its combined influence with lithium on the hydration kinetics, phase evolution, and development of microstructure and molecular structures of hydration products in the blended cement composite was investigated. The experimental and thermodynamic modeling results indicate the synergistic effect between saturated metakaolin and lithium in enhancing the hydration of cement, interaction between metakaolin and cement, incorporation of Al in the silicate chains, and precipitations of Al-rich phases. In the blended cement matrix, the dissolution of metakaolin, formation of calcium silicate hydrates with incorporated aluminum (C-(A)-S-H), and precipitation of strätlingite are improved by 19.6%, 17.6%, and 20.0%, respectively, and the formation of cubic siliceous hydrogarnet was triggered.

1. Introduction

Alkali-silica reaction (ASR) is considered one of the major degradation mechanisms of concrete causing irreparable volume expansion, cracking, substantial damage in concrete structures, and hence significant maintenance costs. Accompanying this challenge is the fact that concrete is the most consumed man-made material and the manufacturing of its binder, cement, is an energy-intensive process responsible for over 8% global CO_2 emissions [1]. Designing durable concrete with high resistance against ASR can not only extend the service life of structures but also decrease the demand for cement thereby possessing long-term impacts to society savings and climate change mitigation. While extensive research efforts have been invested to concrete alkalinity reduction [2], utilization of lithium admixture [3,4], and supplementary cementitious materials (SCMs) [5], these ASR mitigation approaches are only targeted at suppressing one of the prerequisites based on single mechanisms. In addition, these ASR mitigation approaches can inevitably generate deleterious effects on the properties of concrete, such as the decreased workability of concrete [6] and low degree of reaction (DOR) [7] of SCMs at high volume incorporations, as well as the decreased strength [8], accelerated early-age cement hydration, retarded later-age cement hydration, and increased autogenous shrinkage in the presence of lithium admixtures at a lithium to alkali molar ratio (expressed as [Li]/[Na + K]) of 0.74 or higher. These challenges are directly or indirectly correlated to the chemical reactions of the system hence highlighting the urgency to understand the hydration behavior of cement when SCMs or lithium admixtures are incorporated.

As a practical and cost-effective approach, the benefits of internal curing in enhancing the hydration of cement [9], reducing shrinkage [10], mitigating cracking [11], decreasing permeability [12], and hence improving the durability of concrete [13] have been identified in previous studies. A variety of materials, including lightweight aggregates [14], superabsorbent polymer [15], fly ashes [16], coal bottom ash [17], rice husk ash [18], expanded clay [19], and wood pulp fibers [20], have been used as reservoirs to provide additional water to fuel the continuous cement hydration. However, there still exist significant gaps in understanding the efficiency of calcined clay minerals, like metakaolin (MK), in this practical technique. MK possesses a unique structure and pozzolanicity that can result in densified microstructure [21], increased mechanical strength [22], reduced porosity and permeability [23], and improved durability [24,25] of cement, but its extreme water absorption behavior (at least 60% [26]) has been identified as a barrier impairing its reaction degree and cement hydration. This is, in particular, a

* Corresponding author. Department of Civil and Environmental Engineering, University of Massachusetts Lowell, 1 University Avenue, Shah Hall 200, Lowell, MA, USA.
E-mail address: jianqiang_wei@uml.edu (J. Wei).

https://doi.org/10.1016/j.cemconcomp.2023.105268
Received 2 June 2023; Received in revised form 1 August 2023; Accepted 22 August 2023
Available online 23 August 2023
0958-9465/© 2023 Elsevier Ltd. All rights reserved.

challenge in the cement matrix with high volume incorporation of MK as the dissolution of dry MK is found correlating to the concentration of solubilized aluminum thereby affecting the formation rate of stable Al-rich hydration products [27,28]. By leveraging the unique water absorption and desorption behavior of MK, a novel MK-based internal conditioning (MIC) was developed for ASR mitigation in the authors' recent study [29]. Different from lightweight aggregates or superabsorbent polymers, a "duplex" function can be triggered from the clay-based internal curing with a combination of unique pozzolanic reactions and a more uniform distribution of water to enhance cement hydration. In the authors' recent study [29], a desired synergistic effect was observed from the coupling of lithium and saturated MK in mitigating ASR expansion and cracking, which outperforms the single use of lithium and MK in decreasing silica dissolution, suppressing water uptake and swelling potential of ASR gel, as well as converting the expansive ASR (Q^3) gel into non-expansive calcium silicate hydrates (C–S–H) (Q^2) phases.

In light of the promising ASR mitigation effectiveness of the MIC, insights into the hydration kinetics and phase evolutions of cement in the presence of MIC that remain uninvestigated become increasingly crucial to close the loop of this novel technique. Towards this end, this study elucidates the hydration behavior of cement in the presence of MIC tailored by replacing 30 wt% cement with saturated MK nanoparticles with varying degrees of saturation (DOS). The hypothesized coupling effects between the saturated MK and lithium on diminishing the adverse effects of their single incorporations on cement hydration, phase evolution, and development of micro- and molecular structures of the hydration products were investigated. Dynamic vapor sorption (DVS) analysis was performed to understand the moisture absorption and desorption kinetics of the dry and saturated MK nanoparticles. Isothermal calorimetry, thermogravimetric analysis (TGA), X-ray diffraction (XRD), Rietveld refinement, and attenuated total reflection-Fourier transforms infrared spectroscopy (ATR-FTIR) of the hydrated cement systems were performed to obtain comprehensive insights into the cement hydration kinetics, evolutions of hydration products and chemical bonds. Field emission scanning electron microscopy (FE-SEM) along with energy dispersive X-ray spectroscopy (EDS) was performed to determine the micro-morphology and elemental compositions of hydration products. Solid state ^{29}Si and ^{27}Al magic-angle spinning (MAS) nuclear magnetic resonance (NMR) spectroscopy was conducted to understand the structure evolutions of C–S–H and aluminum-bearing phases. Thermodynamic simulations based on Gibbs free energy minimization program (GEMS) [30] were performed to predict the phase assemblage of the cement blends to support the experimental observations.

2. Materials and methods

2.1. Materials

Type I/II ordinary Portland cement (ASTM C150 [31]) (produced by Quikrete), a commonly used type of cement, and MK sourced from South Carolina, a primary kaolin deposit of the United States, were used in this study as cementitious components. The chemical and mineralogical compositions of the cement and MK, analyzed by X-ray fluorescence (XRF) and XRD with Rietveld refinement, are summarized in Table 1. The XRD pattern and corresponding Rietveld refinement of MK are shown in Fig. 1a and b. The content of silicate and aluminate phases ($SiO_2 + Al_2O_3$) in MK is higher than 94 wt%. The water absorption capacity of 61.3% was determined for MK according to ASTM D 281–12 [32], which is in line with previously reported values [26] and will be used for determining the DOS of MK in the following sections. The particle size distributions (PSD) of PC and MK measured by means of laser diffraction are shown in Fig. 1c and d. The cement has a specific surface area and median particle size of 1.66 m^2/g, and 13.8 μm, respectively, while MK has a finer PSD with a specific surface area of 2.93 m^2/g and a median particle size of 3.79 μm. Moreover, reagent grade lithium nitrate with a density of 2.38 g/cm^3 and purity of 99% was used as a lithium source. Extra pure calcium hydroxide (CH) with a purity of 98% and deionized (DI) water were used for mortar sample curing.

Table 1
Chemical and mineralogical compositions of the cement and MK.

	MK (wt.%)	Cement (wt.%)			
CaO	0.071	62.7			
SiO_2	51.8	20.1			
Al_2O_3	42.4	4.8			
SO_3	0.11	3.5			
Fe_2O_3	4.15	3.2			
MgO	–	3.4			
LS	–	1.2			
K_2O	0.218	Equivalent alkali content ($Na_2O + 0.658K_2O$): 0.60			
Na_2O	–	MK		Cement	
TiO_2	1.1	Amorphous	19.03	C_3S	54
ZrO_2	0.088	Kaolinite	73.93	C_2S	17
SrO	0.04	Illite	4.70	C_3A	7
Cl	0.046	Quartz	2.27	C_4AF	10

Note: C_3S: tricalcium silicate; C_2S: dicalcium silicate; C_3A: tricalcium aluminate; C_4AF: tetra-calcium aluminoferrite; LS: limestone.

2.2. Sample preparation

The cement systems with 30 wt% substitutions of cement with MK of varying DOS from 0 to 100%, as well as the addition of lithium nitrate, are summarized in Table 2. In this study, 9 mixture proportions were studied. The matrix with neat Portland cement (PC) and a water to cement ratio of 0.35 was prepared as the control group. Two groups with the addition of low and high lithium in [Li]/[Na + K] ratios of 0.28 (LLi) and 0.74 (HLi) were prepared. Two groups following the conventional use of dry MK with 30 wt% cement replacement (DMK) at the same water to binder (cement + MK, w/b) ratio of 0.35 was prepared by adding a high-performance water reducer admixture (ADVA Cast 555) at a dosage of 0.67% by weight of the binder to address the high water uptake of MK at such a high substitution level to obtained consistent workability. Three groups with 30 wt% cement substitutions with partially saturated MK at DOS of 50% (0.5MIC) and 75% (0.75MIC), as well as 100% fully saturated MK (FMIC), were prepared to study the influence of MIC on cement hydration. The MK was saturated in DI water for 24 h and then dried in an oven at 70 °C until reaching the weight for the specific DOS based on the water absorption capacity of 61.3% determined per ASTM D 281 [32]. Prior to mixing, the MK samples at their desired DOS were sealed for 12 h for moisture homogenization. To identify the benefits of gradually released water from the saturated MK particles, a group with 30 wt% dry MK plus extra mixing water (DMKEW) at the same amount as needed in FMIC, which yields an actual w/b ratio of 0.53, was also prepared for comparison. To explore the coupling effects of saturated MK and lithium on cement hydration, a mixture with coupled incorporation of 30 wt% fully saturated MK and lithium nitrate at a [Li]/[Na + K] ratio of 0.74 (FMIC-Li) was prepared.

Fresh cement pastes for hydration and chemical analysis, including TGA, XRD, ATR-FTIR, and SEM, were mixed in a vacuum mixer at 500 rpm for 3 min. Compared with regular mixing, vacuum mixing is performed under a vacuum condition with a high mixing speed (300–1000 rpm), which favors the homogenization, decreases porosity, and eliminates the carbonation of the cement mixtures during mixing. To understand the hydration behavior of cement under the ambient condition, the pastes were cast in sealed containers conditioned at 25 ± 2 °C (the room temperature) in a vacuum desiccator filled with soda lime to minimize carbonation. At each testing age, the samples for TGA, XRD, and ATR-FTIR tests were ground into fine powders, and the cement hydration was stopped by immersing the powders in anhydrous alcohol for 24 h.

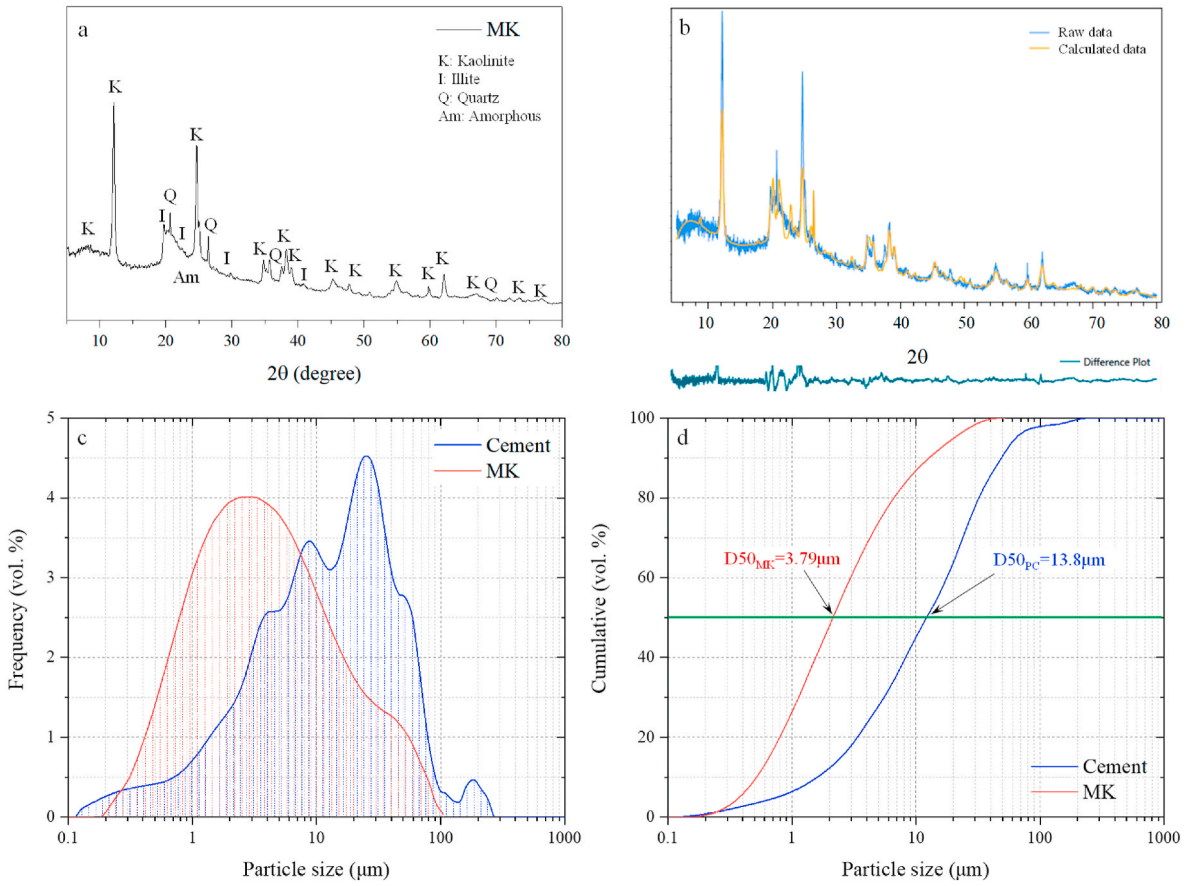

Fig. 1. (a) XRD patten and (b) Rietveld refinement of MK, and particle size distributions of the cement and MK: (c) the relative frequency of particles based on diameter, and (d) volume of the particles smaller than a certain diameter.

Table 2
Compositions of cement mixtures.

Index	Content (g)							w/b ratio
	Cement	Mixing water	Lithium nitrate	MK	Water for MIC	DOS of MK	Superplasticizer	
PC	100	35	–	–	–	–	–	0.35
LLi	100	35	0.3756	–	–	–	–	0.35
HLi	100	35	0.9880	–	–	–	–	0.35
DMK	70	35	–	30	–	0	0.67	0.35
DMKEW	70	53	–	30	–	0	–	0.53
0.5MIC	70	35	–	30	9.14	50%	–	0.35
0.75MIC	70	35	–	30	13.73	75%	–	0.35
FMIC	70	35	–	30	18.24	100%	–	0.35
FMIC-Li	70	35	0.6916	30	18.24	100%	–	0.35

2.3. Test procedures

2.3.1. Dynamic vapor sorption of MK

As the basis of MIC, the moisture sorption behavior of MK plays a critical role in understanding its potential to modify cement hydration by providing gradually released water. In this study, the moisture absorption and desorption behavior of both dry and fully saturated MK were characterized at 25 °C via DVS analysis using a DVS INTRINSIC II system (Surface Measurement System LTD). Powdered MK samples with a weight of approximately 20 mg were tested by monitoring their mass changes at varying relative humidity (RH) controlled by the modulation between flows of dry N_2 and HPLC grade water vapor. For dry MK, the absorption behavior was tested first from an initial RH of 0, which was increased to 90% with a 10% increment, followed by a 5% increment to 95% RH. The desorption process was measured by decreasing the RH back to zero with the same step sizes. Reversed humidity steps were followed, i.e., 95% to 0 and then back to 95% RH, for the fully saturated MK so that the desorption was measured first, followed by an absorption measurement. The data points, including the mass, temperature, and RH, were collected in 1 min time intervals. For each RH step, equilibrium was considered to be reached when the mass change rate is less than 0.002% per minute over a period of 5 min, from where sorption isotherms were determined by plotting equilibrium mass as a function of RH.

2.3.2. Isothermal calorimetry

To monitor the heat flow and release of cement hydration, as well as the influences of lithium nitrate and MIC in hydration kinetics of cement, isothermal calorimetry was performed at 25 °C during the first 50 h of hydration using an I-Cal 2000 HPC High Precision Isothermal Calorimeter. For each measurement, the raw materials, i.e., cement, dry or saturated MK, lithium nitrate, and mixing water, were conditioned in

the calorimeter chambers at the target temperature of 25 °C for 24 h. The mixing of 50 g paste samples at a temperature of 25 ± 2 °C was done within 1 min immediately followed by sealing in plastic containers and monitoring of hydration heat.

2.3.3. TGA

To characterize the influences of lithium nitrate, MIC and their combination on the evolutions of cement hydration products, TGA was carried out on ground powders of hydrated cement pastes after 1, 7, 14, 28, and 90 days using a PerkinElmer TGA 4000 thermogravimetric analyzer. A heating rate of 15 °C/min from 30 °C to 800 °C under N_2 purge gas at a flow rate of 20 mL/min was applied. The contents of CH and $CaCO_3$ (CC) in the pastes, corresponding to the weight loss between 400 °C and 510 °C, and 590 °C–710 °C based on the tangent method [33] (it is worth noting that the temperature boundaries of portlandite and calcite slightly vary for each sample, i.e., the temperature ranges were determined via the tangent method, instead of fixed values), respectively, were determined by using:

$$CH_1 = [(W_{400} - W_{510}) / W_{510}] \times M_{Ca(OH)_2} / M_{H_2O} = [(W_{400} - W_{510}) / W_{510}] \times 4.1 \times 100\% \quad (1)$$

$$CC = [(W_{590} - W_{710}) / W_{710}] \times M_{CaCO_3} / M_{CO_2} = [(W_{590} - W_{710}) / W_{710}] \times 2.27 \times 100\% \quad (2)$$

where CH_1 and CC are calcium hydroxide and calcium carbonate contents, W_n is the mass at temperature n °C, M is the molar mass. Again, the temperatures for CH and CC thermal decomposition were determined based on a tangent method rather than fixed values. The small amount of CC was considered mainly due to the carbonation of CH during the process of sample preparation although the carbonation has been minimized during sample preparation. Thus, in this study, the total CH content precipitated in the cement pastes was calculated by summing the CH_1 in Eq. (1) and the CH_2 converted from CC as follows:

$$CH = CH_1 + CC \times \frac{M_{CaCO_3}}{M_{Ca(OH)_2}} = CH_1 + CC \times 0.74 \quad (3)$$

where CH is the portlandite converted from CC.

The non-evaporable water content (W_{ne}) of the cement blends was calculated based on the weight loss between around 115 °C and around 510 °C on TGA curves by using Eq. (4). Again, the temperature boundaries here are not fixed, which may slightly vary for each sample based on the tangent method.

$$W_{ne} = (W_{510} - W_{115}) / W_{510} \times 100\% \quad (4)$$

It should be noted that MK can react with CH due to its highly pozzolanic reactivity to form additional C–S–H, C_4AH_{13}, C_3AH_6, and C_2ASH_8 [34]. The work by Dunster et al. [34] revealed that a full reaction of 1 g MK can consume 1.6 g CH and produce 0.4 g non-evaporable water. Thus, as shown in Eq. (5), instead of being determined from TGA curves, the content of CH in the cement-MK blends can also be theoretically determined by subtracting the MK-consumed CH from the CH formed from cement hydration [35]. In the same way, the non-evaporable water content in the cement blends containing MK is the result of the non-evaporable water from the cement hydration and the one formed from the pozzolanic reaction induced by MK. Therefore, the CH consumption ($\nu_{MK} = 1.6$) and the non-evaporable water produced by 1 unit mass fully reacted MK ($W_{MK} = 0.4$) determined from Ref. [34] were taken into account in the calculations of CH contents (Eq. (5)) and non-evaporable water contents (Eq. (6))

$$CH = CH_{PC} \bullet f_C \bullet DOH_{PC} - \nu_{MK} \bullet DOR_{MK} \bullet f_{MK} \quad (5)$$

$$W_{ne} = W_{PC} \bullet f_C \bullet DOH_{PC} + W_{MK} \bullet DOR_{MK} \bullet f_{MK} \quad (6)$$

where CH_{PC} is the CH produced from the hydration of 1 unit mass of fully hydrated cement ($CH_{PC} = 0.32$ as calculated from GEMS); ν_{MK} is the CH consumed from the reaction of 1 unit mass of fully reacted MK ($\nu_{MK} = 1.6$ [34]); DOH_{PC} and DOR_{MK} represent the reaction degrees of cement and MK, respectively; f_C and f_{MK} are the mass fraction of cement and MK in the blends, respectively. Thus, in a blended cement system, $CH_{PC} \bullet f_C \bullet DOH_{PC}$ represents the amount of CH produced from cement hydration, and $\nu_{MK} \bullet DOR_{MK} \bullet f_{MK}$ is the amount of CH consumed by the MK reaction. W_{PC} and W_{MK} are the contents of non-evaporable water produced by 1 unit mass fully hydrated cement ($W_{PC} = 0.25$ [36,37]) and 1 unit mass fully reacted MK ($W_{MK} = 0.4$ [34]), respectively. Therefore, $W_{PC} \bullet f_C \bullet DOH_{PC}$ and $W_{MK} \bullet DOR_{MK} \bullet f_{MK}$ are the contents of the non-evaporable water produced from the hydration of cement and the pozzolanic reaction of MK, respectively.

For each blended cement system, the degree of hydration (DOH) of cement (DOH_{PC}) can be determined by merging Eqs. (5) and (6), whereby the DOR of MK (DOR_{MK}) can be canceled out and the DOH_{PC} can be obtained:

$$DOH_{PC} = (CH + 4W_{ne}) / (1.32 \bullet f_C) \quad (7)$$

Based on the CH and DOH_{PC}, the DOR_{MK} can be derived as follows:

$$DOR_{MK} = [CH_{PC} \bullet f_C \bullet DOH_{PC} - CH] / 0.4 \quad (8)$$

2.3.4. XRD and ATR-FTIR

To understand the evolutions of the crystalline phases produced in the cement, XRD investigation was performed on ground powders after 7, 28, and 90 days of hydration using an AXRD powder X-ray diffractometer at 30 kV and 20 mA. To obtain accurate XRD patterns for Rietveld refinement, the cement samples were scanned on a rotary support in stepwise mode with a step size of 0.02° (2θ) with a scanning time of 5 s per step. The obtained XRD data was analyzed using the XRDWIN®PD software combined with the Crystallography Open Database (COD). The phase assemblages of the hydrated cement paste powders, including both amorphous and crystalline ones, were quantified by XRD-Rietveld refinement using the built-in Whole-Pattern Fitting in XRDWIN®PD. A 7th order of Chebyshev polynomial background removal was applied to separate the crystalline and amorphous phases from the XRD data. During the refinement, the Voigt model was used to fit the peaks with a full profile fitting procedure to overcome the problem of peak overlapping [38]. Reference crystallographic index files (CIF) of portlandite (#1001787), hydrogarnet (#1007235), crystalline C–S–H (calcium chondrodite: #1529964, suolunite: #1542055, tobermorite: #8103550), crystalline calcium aluminate silicate hydrate (C-(A)-S-H) (Al-tobermorite: #1527001, heulandite: #1534144, gismondine: 1557940), anhydrates (C_2S: #9012794, C_3S: #1540704, gypsum: #1011074), ettringite (#9011103), strätlingite (#9005059), and zeolite (#1530654) were used in the refinement analysis. The profile R-factor (also known as the residual factor), the most straightforward index for a fitting criterion defined in Eq. [9,39], was used to represent the difference between the experimental raw and ideally computed values, where a lower R-value indicates a better refinement fitting, and it is normally considered a desirable target with R ≤ 0.2 [40].

$$R = \frac{\sum||F_{obs}| - |F_{calc}||}{\sum|F_{obs}|} \quad (9)$$

where F_{obs} and F_{calc} are the observed and calculated structure factors.

To determine the formation of chemical bonds in the reaction products, ATR-FTIR spectra of the ground cement paste powders after 7, 28, and 90 days were recorded with a Thermo Fisher Scientific Nicolet iS10 FTIR spectrometer. The spectra between 4000 and 400 cm^{-1} with a resolution of 4 cm^{-1} were acquired based on a co-addition of 32 scans with a scanning time of 52 s.

2.3.5. ^{29}Si and ^{27}Al MAS NMR spectroscopy

Solid state ^{29}Si and ^{27}Al MAS NMR were conducted on ground powders of the selected paste after 650 days of hydration to determine the molecular structures of the main reaction products, such as C–S–H. The spectra were recorded on a Bruker Neo501-500 MHz NMR spectrometer with a two-channel 3.2 mm MAS probe. The powder samples were packed into a zirconia rotor spinning at 10 kHz. An NMR frequency of 99.37 MHz and 130.35 MHz was obtained by the magnet field of 11.7 T for characterizing the local atomic structure of ^{29}Si and ^{27}Al, respectively. The single-pulse tests were employed with a 45° excitation pulse. To ensure obtaining sufficient intensity of the characteristic spectra peaks based on the probe size, the ^{29}Si spectra were made up of 1024 scans with a relaxation time of 10 s in relation to tetramethylsilane and the ^{27}Al spectra were collected based on 512 scans with a relaxation time of 2 s using aluminum nitrate hydrate ($Al(NO_3)_3{\cdot}9H_2o$) as the reference. Spectral deconvolution of both ^{29}Si and ^{27}Al MAS NMR was performed using MestReNova by employing the Lorentzian-Gaussian shape function. The intensity of ^{27}Al peaks was used to evaluate the evolutions of Al-bearing phases, such as the third aluminate hydrates (TAH), hydrogarnet, monosulfate (AFm), ettringite, C-A-S-H, and strätlingite, as well as the unhydrated belite, and alite. The relative intensities of the Si sites from the ^{29}Si spectra were used to determine the polymerization degree (PD), mean molecular chain length (MCL), hydration degree (HD), the average chain lengths of pure silicate units (SU), average chain length of aluminosilicate tetrahedra (AT), and the average Al/Si molar ratio ($R_{Al/Si}$) in the chains of tetrahedral (Al incorporated into the silicate chains of C–S–H) by following Eqs. [10–15], respectively:

$$PD = Q^2/Q^1 \quad (10)$$

$$MCL = 2\left(Q^1 + Q^2\right)/Q^1 \quad (11)$$

$$HD = \left(Q^1 + Q^2\right) \Big/ \left(Q^0 + Q^1 + Q^2\right) \quad (12)$$

$$SU = 2\left(Q^1 + Q^2 + Q^3(1Al)\right)/\left(Q^1 + Q^3(1Al)\right) \quad (13)$$

$$AT = \left(2Q^1 + 2Q^2 + 3Q^3(1Al)\right)/Q^1 \quad (14)$$

$$R_{Al/Si} = Q^3(1Al)/\left[2\left(Q^1 + Q^2 + Q^3(1Al)\right)\right] \quad (15)$$

where Q^0 is the relative area of the Si sites in the anhydrates (i.e., alite and belite); Q^1, Q^2, and $Q^3(1Al)$ are the ones for the Si sites in the C–S–H/C-A-S-H phases.

2.3.6. Micro-morphology

The microstructure of the cement pastes after 100 days of hydration was investigated on selected samples using a JEOL JSM 7401F FE-SEM under an accelerating voltage of 10.0 kV. The main hydration products, such as C-(A)-S-H, ettringite, and portlandite, were morphologically characterized. The sample surfaces were made conductive by sputtering the deposition of a thin layer of gold using a Denton vacuum sputter coater. The elemental quantification of the hydration products was collected through an EDS Genesis XM2 imaging system consists of a 10 mm^2 Si (Li) detector with a SUTW window under an accelerating voltage of 15.0 Kv.

2.3.7. Thermodynamic modeling

Thermodynamic modeling was carried out for the cement pastes using GEMS with a CEMDATA18.1 supplemental database for cementitious phases to calculate the equilibrium phase assemblages and speciation precipitation from the total bulk elemental compositions. Seven main components of cement, including CaO, SiO_2, Al_2O_3, Fe_2O_3, MgO, K_2O, SO_3, and three main compositions of MK, i.e., SiO_2, Fe_2O_3, and Al_2O_3, were selected as inputs for simplicity. The water in saturated MK was also taken into account as water input. Two simulations, one predicting phase assemblages over time based on the calculated DOH of cement and DOR of MK, and one predicting phase assemblages as a function of MK reaction degree at an assumed cement DOH of 80%, were performed.

3. Results and discussion

3.1. Dynamic vapor sorption kinetics of MK

The water vapor absorption and desorption kinetics and sorption isotherms of dry MK in a full wetting and drying cycle are presented in Fig. 2a and b, respectively. Both absorption and capillary condensation, the two types of physically bound water [41], were observed from MK. The absorption occurs through the whole RH range up to saturation, which is due to the adsorbed water on the surface of clay particles, while the capillary condensation is due to the filling of pores in clay particles driven by the thermodynamic forces, which only happens at the relative high RH levels [42]. From the dry condition (RH = 0) to 70% RH, the dry MK exhibited slight water vapor absorption with a mass increment of 0.05%–0.10% for each of the RH steps. Similar mass variations (0.06%–0.15%) were also observed from the desorption procession from 70% RH to 0% RH. This indicates that only absorption occurred in the RH range lower than 70%. As shown in Fig. 2a, as the RH increased, more significant water absorption was exhibited. At 80%, 90%, and 95% RH, the equilibrium mass changes were 0.29%, 1.03%, and 2.09%, respectively, yielding a maximal moisture uptake of 3.88% by the mass of the dry MK. During the drying process, more than 73% of the moisture was desorbed when the RH dropped from 95% to 80%. As shown in Fig. 2b, the vapor sorption isotherm of dry MK can be categorized as type II absorption patterns due to the combination of adsorbent–adsorbate and adsorbate–adsorbate interactions per the International Union of Pure and Applied Chemists (IUPAC) [43] in 1985, which can be divided into three segments [44,45]: (1) the monolayer absorption at the RH below 10%; (2) the multilayer absorption segment with a linear low-gradient curve between 10% and 70% RH; and (3) pore condensation at higher RH. The inflection point at the beginning of the isotherm, i.e., at 10% RH, indicates the transformation from monolayer absorption to multilayer moisture absorption. A rapid increase in water absorption between 70% and 95% RH was identified from the sorption isotherm, which suggests the dominant capillary condensation triggered by the porous and multilayered characteristics of MK. The significant moisture absorption and desorption of MK, especially at RH higher than 70%, demonstrate the great potential of this calcined clay mineral as an internal conditioning agent.

Different from dry MK, the fully water-saturated MK (100% DOS) exhibits a dramatic weight loss at 95% RH (see Fig. 3a), which is 11 times the total weight loss of dry MK during its drying cycle. This is due to the significant difference between water saturation and moisture wetting. As the RH decreased from 95% to 90%, a 42.92% weight loss was obtained, which is 26 times the mass change of dry MK in the same desorption step. The maximum moisture uptake of saturated MK during its wetting cycle is 4.3%, which is higher than that of dry MK. As the interlayer and pores of MK were enlarged in the water saturation process, the moisture is mainly absorbed on the surface or into the interlayer and pores of the absorbent [46]. Nevertheless, the isotherm of the

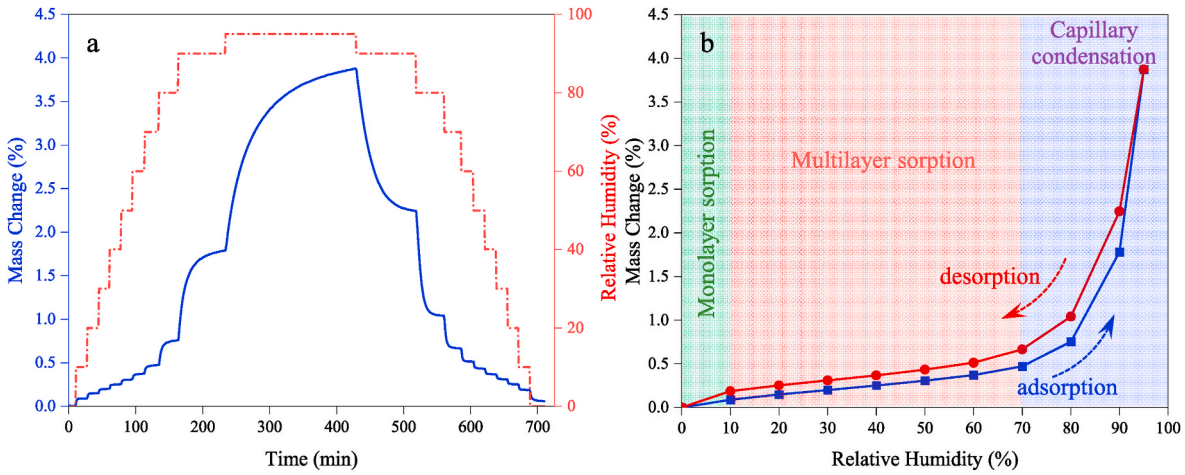

Fig. 2. Water vapor sorption kinetics (a) and sorption isotherm (b) of dry MK.

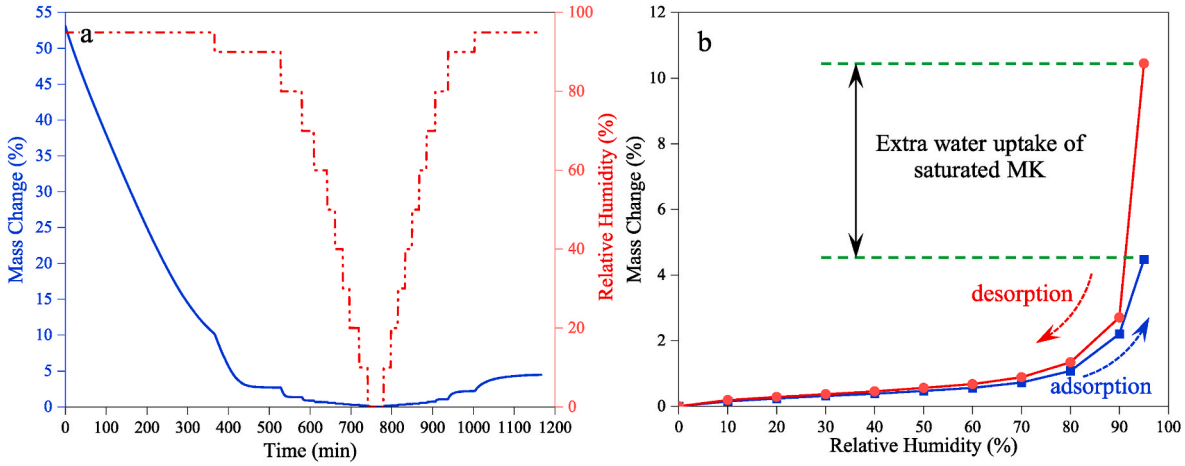

Fig. 3. Water vapor sorption kinetics (a) and sorption isotherms (b) of 100% DOS MK.

saturated MK was not looped due to the large difference between and initial and final equilibrium mass. This difference in equilibrium mass at 95% indicates the significant water uptake capacity of MK exceeding vapor absorption. According to Ref. [43], the absorption isotherm of the saturated MK is in line with the type III sorption pattern dominated by adsorbate–adsorbate interactions as there is no inflection point, the absence of which indicates that the monolayer was not formed and the moisture was mainly absorbed on the surface of the macroporous particles [47]. As shown in Fig. 3b, the saturated MK exhibited a lower hysteresis between absorption and desorption isotherms than dry MK indicating that the micropores or interlayer of MK have been expanded by the saturation with less ink-bottle effect, which acts as a "bottleneck" for the inner large space accessible through narrow necks to protect drying during desorption [48]. The lower sorption hysteresis and the absence of pore condensation suggested the expansion of MK after saturation and its effective role as a water carrier in internal curing to provide both additional curing water and pozzolanic reaction to the matrix of cement.

3.2. Calorimetry studies

The calorimetric measurements on neat PC, binary cement blends with lithium nitrate or MIC, and trinary cement blends with coupled saturated MK and lithium normalized by the weight fraction of cement are shown in Fig. 4a–d. The classic five-stage heat flow curves were identified from all the groups with varying values and rates. Due to the rapid hydration of C_3A beginning immediately upon wetting [49], extreme exothermicity in the initial (pre-induction) stage was observed. From PC, two peaks were observed from its heat flow curve at 7 and 8.5 h during the acceleration and deceleration stages, indicating the reaction of silicate and secondary hydration of tricalcium aluminate. A subsequent broad shoulder corresponding to the conversion of ettringite to AFm phases was also observed between 20 and 30 h in the stage of the slow continued reaction.

From Fig. 4a, accelerated early-age cement hydration in the presence of lithium was observed. By adding 0.28 lithium, the peaks corresponding to silicate and secondary aluminate reactions overlapped with a higher amplitude. When the dosage of lithium was increased to 0.74, not only the amplitude of the peak was further raised, but also the exothermic peak occurred earlier indicating the enhanced initial cement hydration. The same phenomenon was also observed from the cumulative heat release curves in Fig. 4b, wherein more early-age hydration heat was released from the cement with lithium. However, after 24 h, the hydration heat released from neat PC exceeded LLi and HLi suggesting the retarded reactions in the presence of lithium, which is in agreement with the findings by Millard and Kurtis [50]. With the incorporation of MK, due to the high aluminate content, the pre-induction stage ended slightly later than the neat PC and cement-lithium blends. Although the occurrence of the exothermic peak was not moved earlier, a higher and narrower peak with a larger slope of acceleration stage exceeding both PC and cement-lithium blends (LLi and HLi) was observed. This indicates the positive role of MK

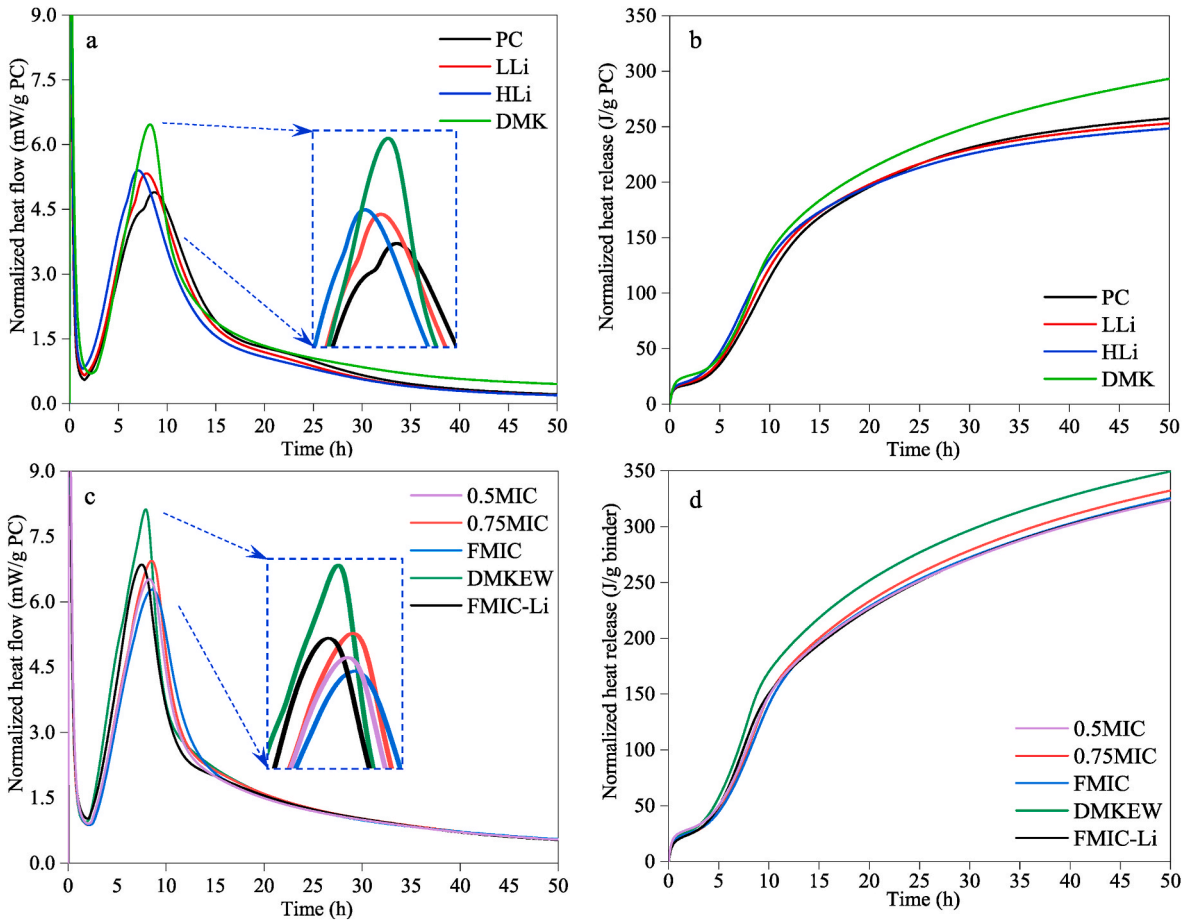

Fig. 4. Normalized specific heat flow and heat release of the cement blends.

nanoparticles in the formation of C–S–H by providing additional nucleation sites [51]. More importantly, the aluminate peak corresponding to sulfate depletion was effectively enhanced and accelerated. The high aluminate content of the MK particles redefined the Al/Si ratio of the cement system and altered the reactivity of the aluminate phases. Due to the dilution effect, the total heat output of the cement-MK blends is lower than that of PC, but the normalized hydration heat is higher with a total heat increase of 13.9% after 50 h. The comparison among the groups reveals that, with different mechanisms, the incorporation of 30 wt% MK can improve the hydration of cement more effectively than lithium.

The influences of saturated MK on the hydration heat of cement can be found in Fig. 4c and d. From Fig. 4c, compared with the groups with saturated MK, the DMKEW exhibited a higher heat flow peak. This is due to the high availability of free mixing water that can enhance initial cement hydration by promoting effective contact between water and clinker grains. However, this higher w/b ratio (0.53) can generate a more porous structure in the cement matrix with lower mechanical strength and aging resistance. Comparing the DMK (Figs. 4a), 0.5MIC did not yield higher heat flow peaks but resulted in an increased amount of heat release. When the DOS of MK was increased from 50% to 75%, a higher exothermic peak was obtained from 0.75MIC, while a further increased DOS to 100%, i.e., FMIC, resulted in a lower and wider heat flow peak. It should be noted that, in the period of slow continued reaction, the heat flow is positively correlated to the DOS of MK indicating the positive role of the gradually released water in long-term cement hydration. As shown in Fig. 4d, the heat release of the FMIC group exceeded 0.5MIC after 15 h, but it is still lower than that of 0.75MIC up to 50 h. Compared with HLi and FMIC, FMIC-Li exhibited an earlier and higher heat flow peak. This observation indicates the synergistic effects between lithium and saturated MK in cement hydration that the accelerated early-age cement hydration remained but the retarding effect of lithium on later-age cement hydration can be offset.

3.3. Characterization of hydration products

3.3.1. Thermogravimetric analysis

Fig. 5 shows the TGA and DTG curves of the cement pastes after 1 day and 90 days of hydration. Additional analyses of TGA and DTG curves obtained at 7 days, 14 days, and 28 days can be found in Appendix A. The weight losses at varying temperature ranges shown in the TGA curves, as well as the corresponding peaks of the DTG curves in the same temperature ranges, are attributed to thermal decompositions of hydration products [52], such as evaporable water in the range of 30–115 °C [53], ettringite in the range of 110–170 °C [54], non-evaporable water from C–S–H partially overlapped with ettringite and/or strätlingite at ~200 °C [55], AFm in the range of 250–300 °C [56], CH (portlandite) between 400 °C and 510 °C [57] and CC (calcite) [7] in the range of 590–710 °C. From Fig. 5a and b, it can be seen that the weight losses of ettringite and C–S–H increased with the amount of lithium at 1 day. This confirmed the role of lithium in accelerating early-age cement hydration. However, less ettringite and C–S–H can be detected from LLi and HLi at later ages (Fig. 5c and d, and A1) due to the retarded cement hydration in the presence of lithium. This finding is consistent with the calorimetry results above and agrees well with the retarded effect of lithium observed in previous studies [50,58]. For the groups containing MK, more ettringite was formed than PC initially. However, the ettringite contents of the MK-groups decreased over time and became lower than that of the control group, demonstrating the enhanced AFm formation in the later ages, which was also observed

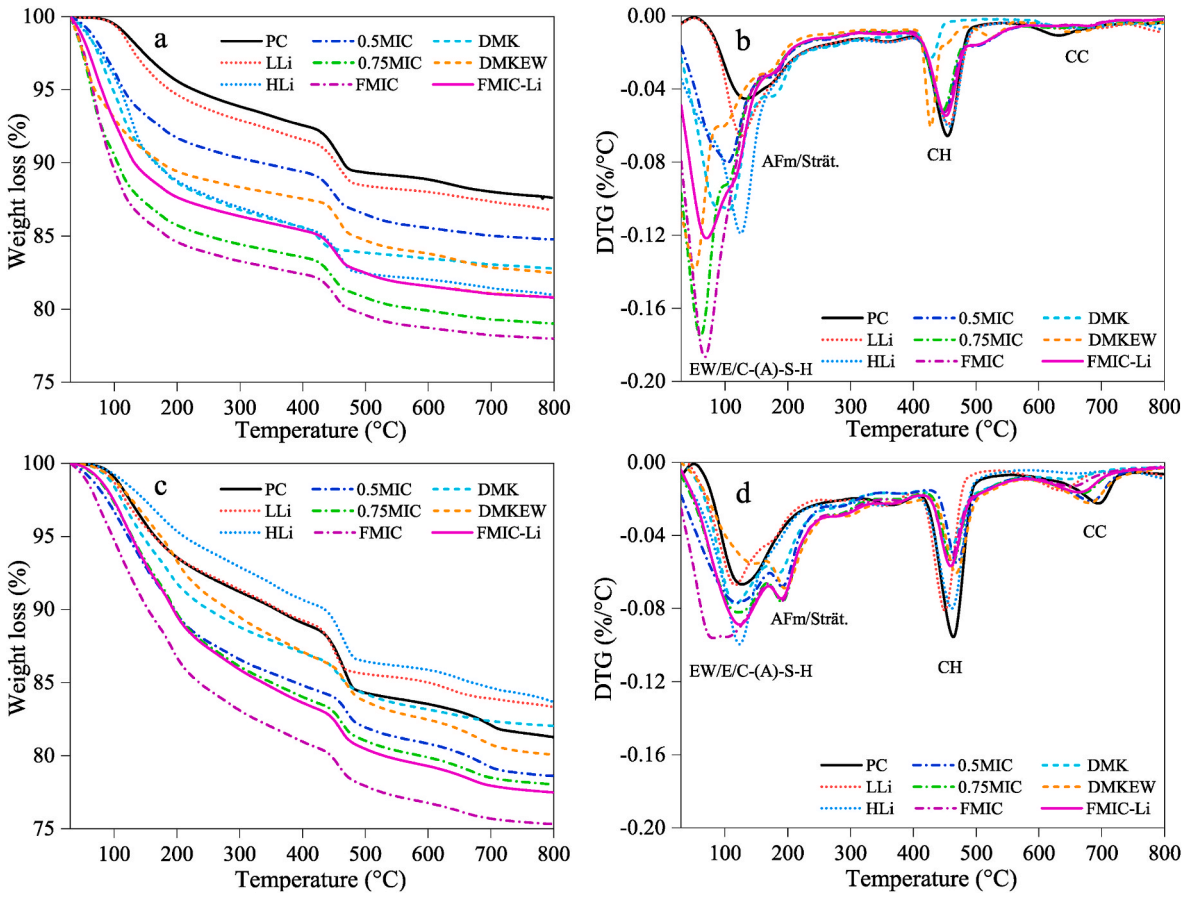

Fig. 5. TGA curves of cement pastes at (a, b) 1 day and (c, d) 90 days. EW-evaporable water, E-ettringite, CH-portlandite, Strät-strätlingite, CC-calcite.

from the calorimetry analysis (see Fig. 4). For the decomposition of AFm phases, both LLi and HLi presented identical mass loss with the control group. Agreeing well with the findings of AFt, compared with PC, less AFm was formed from the groups containing MK on the first day. However, the content of AFm was found to increase over time, which is in line with the formation of C–S–H phases indicating the enhanced cement hydration accompanied with the formation of additional hydrates due to the pozzolanic reactions. The DMK group shows the lowest amount of evaporable water among all the groups. Due to the extra mixing water, DMKEW exhibited more evaporable water than the control group. The higher evaporable water contents in LLi and HLi might be induced by the retarded cement hydration, while the higher evaporable water contents from the groups with saturated MK were mainly due to the higher water amount in the saturated MK. With progressive hydration, the amount of C–S–H was also observed to increase over time for all the groups. After 90 days of hydration, LLi and HLi showed slightly lower C–S–H decomposition peaks than PC, while additional mass losses due to the dehydration of C–S–H were observed from the groups with MK. Comparing with DMK and DMKEW, a more significant CH decrease was observed from the FMIC indicating the sustained pozzolanic reaction of MK in the presence of the gradually released extra water via MIC. While FMIC-Li exhibited a lower peak below 100 °C due to the lower amount of free water than FMIC, it showed the most significant AFm and C–S–H decomposition among the groups. This observation plus the findings from calorimetry provide an indication that a synergistic effect between lithium and the saturated aluminum-rich MK might exist in enhancing the hydration of portland cement.

The development of CH content in the cement systems as a function of hydration time determined through Eqs. (1)–(3) is illustrated in Fig. 6. The PC showed a relatively high CH content of 13.9% after 1 day, which increased to 17.5% after 28 days. The CH contents of LLi and HLi are

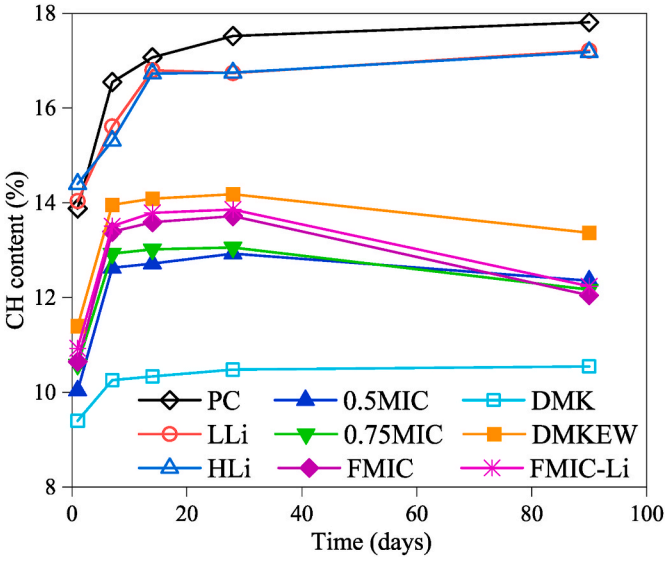

Fig. 6. Calcium hydroxide contents determined by TGA.

14.0% and 14.4% on the first day, respectively, which are 0.7% and 3.6% higher than that of PC, providing another indication for the enhancement of early-age cement hydration with lithium after the calorimetry test. However, after 7 days, the CH contents in these two lithium groups increased to 15.6% and 15.3%, which are 5.7% and 7.5% lower than PC, respectively. This reveals the retardation of cement hydration after 24 h. Nevertheless, it was found that the evolution of CH in

LLi and HLi showed a decreasing distinction over time from 0.3% at 7 days to 0.03% at 90 days. This confirmed the faded retarding effect of lithium on cement hydration at later ages.

Different from the reaction retardance caused by lithium, the incorporation of MK resulted in more efficient CH consumption. The CH contents of DMK at 1 day and 7 days are 9.4% and 10.3%, respectively, which are 32.3% and 38.0% lower than PC. This is not only due to the dilution effect by partially replacing cement but also the effective CH consumption of MK through pozzolanic reactions [51,59] as indicated by the formations of additional hydration products, such as C–S–H, C-A-S-H, AFm, and strätlingite, detected from the TGA (see Fig. 5 and A1) and XRD (Fig. 8) analyses. It was observed that the blended cement groups with saturated MK yielded more CH than DMK at all the investigated five ages and the CH content increased with the DOS of MK. It's interesting to note that, different from the continuously increasing CH content observed from PC, LLi, HLi, and DMK, decreasing CH contents were obtained from the cement blends with MIC (0.5MIC, 0.75MIC, FMIC, and FMIC-Li) and the decreasing rate of CH content showed a positive correlation with the DOS of MK. As a result, the correlations between MK DOS and CH content in the cement systems were reversed at 90 days, i.e., less CH was detected from the groups with higher MK DOS. These observations indicate that the gradually released water induced by saturated MK not only enhanced the hydration of cement but also improved the pozzolanic reactions to consume more CH at later ages. With the same total amount of water, DMKEW shows a higher CH content than FMIC, which shared the same total amount of water in different forms indicating the superior role of MIC in modifying cement hydration. The acceleration effect of lithium on cement hydration during the first day was also observed in FMIC-Li. From 1 day to 90 days, the combined incorporation of lithium and saturated MK showed a slightly higher CH content than FMIC with an invariable difference. This might be due to the acceleration of cement hydration in the first 24 h triggered by lithium and its less effect on the pozzolanic reaction.

The development of non-evaporable water in the cement blends as a function of hydration time is shown in Fig. 7a. It is seen that a major fraction of the chemically bounded water was detected during the first 28 days for all the groups, and only a slight increase was detected at later ages indicating the early occurrence of most of the hydration reactions. In line with the development of CH, two distinguishable levels of non-evaporable water contents were identified: (i) a low level with a slow increase rate in PC, LLi, and HLi, and (ii) a high level with a rapid initial increasing rate in the cement blends with dry MK and MIC. PC yielded a non-evaporable water content of 43.4% and 69.9% after 1 day and 14 days, respectively, and only a slight increase of 3.1% was observed from 14 days to 90 days. Due to the accelerated cement hydration induced by lithium, the non-evaporable water contents of LLi and HLi were 7.7% and 35.3%, respectively, higher than PC after 1 day. However, after 7 days of hydration, due to the retarding effect of lithium, the differences were decreased to 5.8% and 20.8%. Thereafter, conversed results that share the same trend of CH contents (see Fig. 6) were observed. At 14 days, compared with PC, LLi showed 1.6% higher non-evaporable water content, while HLi yielded 2.5% less. After 28 days, the non-evaporable water contents of LLi and HLi tend to be comparable, and both became lower than that of PC. This is strong evidence for the retarding effect of lithium on later-age cement hydration with fewer C–S–H, ettringite, and AFm phases as shown in the TGA analysis (see Fig. 5 and A.1).

A significant increase in non-evaporable water content due to the incorporation of MK was observed from the DMK, which indicates the enhanced cement hydration and the resultant formation of additional water-rich phases due to pozzolanic reactions in line with the findings of Vance et al. [60] and Gbozee et al. [61]. The cement blends with saturated MK exhibited higher non-evaporable water contents than DMK, and this enhancement increases with the DOS of MK. After 28 days, 0.5MIC, 0.75MIC, and FMIC showed non-evaporable water contents of 23.4%, 24.1%, and 25.5%, respectively, which are 3.5%, 6.6%, and 12.8% higher than that of DMK. These increments became more significant at 90 days. Although with the same total amount of water, FMIC yielded a higher content of non-evaporative water than DMKEW. This again confirms that MIC induced by saturated MK works more effectively than the conventional direct incorporation of dry MK in enhancing cement hydration. More interestingly, FMIC-Li showed the highest amount of non-evaporable water among all the groups up to 90 days of hydration, which confirms the synergistic role of lithium and saturated MK in enhancing cement hydration.

Fig. 7b illustrates the developments of DOH of cement (DOH_{PC}) in each group at different ages, which was estimated from the development of non-evaporable water and CH contents according to Eq. (7). For PC, the DOH_{PC} increased from 43.4% at 1 day to 73.0% at 28 days, while only an increase of 0.06% from 28 days to 90 days was observed. In LLi and HLi, the first-day cement hydration was accelerated by 3.3% and 15.3%, respectively. Thereafter, this influence declined, especially for HLi, which became 3.4% lower than PC after 28 days. From the evolution of the chemically bonded water content, the first-day accelerating effect and late-age retarding effect are both positively correlated to the lithium dosage. As a result, the DOH_{PC} in LLi became higher than that of HLi from 14 days. Agreeing well with the evolution of CH content (Fig. 6), the difference in DOH_{PC} between LLi and HLi decreased over time, which again indicates the fading influence of lithium and its dosage on later-age cement hydration. A significant enhancement was observed from DMK, which yielded a DOH of 58.3% on the first day comparable to that of HLi. In contrast to lithium, no retarding effect on later-age cement hydration was observed from MK. The 7-day DOH_{PC} in DMK increased to 78.6%, which is 38.4% higher than that of PC, followed by a 4.8% further increase at 90 days. This low increment after 7 days might be due to the lack of water for cement hydration due to the extreme absorption feature of the dry MK particles. The superiority of saturated MK outperforming the conventional direct incorporation of dry MK can be observed from the evolution of DOH from 7 days. 14-day

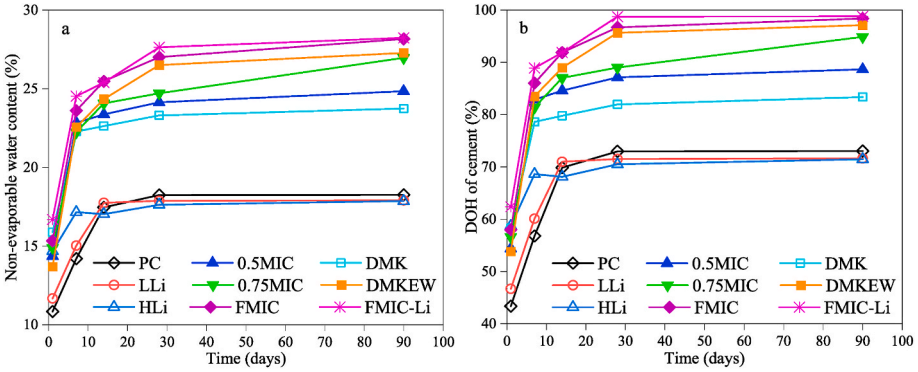

Fig. 7. The developments of (a) non-evaporable water content and (b) DOH for cement in the cement blends.

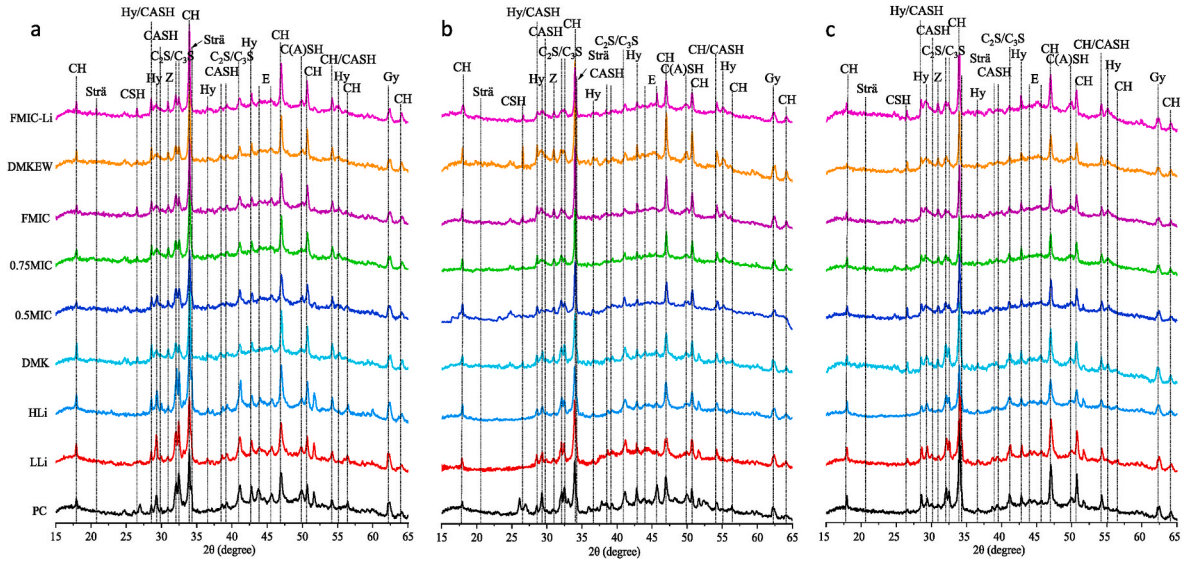

Fig. 8. XRD patterns of the hydrated cement matrixes after (a) 7 days, (b) 28 days, and (c) 90 days (CH: calcium hydroxide, C: calcite, Ett: ettringite, Strä: strätlingite, C–S–H: calcium silicate hydrates, C-A-S-H: calcium aluminum silicate hydrates, Z: zeolite, Hy: hydrogarnet, Gy: gypsum).

cement DOHs of 84.6%, 87.0%, and 91.9% were obtained from 0.5MIC, 0.75MIC, and FMIC, respectively, which are 3.2%, 6.1%, and 12.1% higher than that of DMK. These differences were further increased to 6.4%, 13.8%, and 18.0% after 90 days. In striking contrast, DMKEW showed 1.1%–7.2% lower DOHs of cement than FMIC during the entire testing period (1 day–90 days) although the two groups had the same total amount of water. This revealed that the gradually released water from saturated MK plays a more effective role than free mixing water in fueling the continuous cement hydration reactions. Due to the synergistic effect between lithium and saturated MK, eliminated retarding effect of lithium on cement hydration was detected in FMIC-Li, which yielded the highest DOH of cement among all the groups up to 90 days. At 1 day, the DOH_{PC} in FMIC-Li was 46.2%, 8.0%, and 9.3% higher than that of PC, HLi, and FMIC, respectively, and these distinctions became 35.2%, 38.2%, and 0.4% at 90 days. Matching up with the observations in non-evaporable water content, these findings suggested that the negative effect of lithium on later-age cement hydration and phase evolution can be completely offset by MIC via coupled incorporation.

3.3.2. X-ray diffraction and rietveld refinement

Fig. 8 presents the XRD patterns of the hydrated cement pastes after 7 days, 28 days, and 90 days. From the XRD patterns of PC, ettringite, C–S–H, C-A-S-H, hydrogarnet, and an increasing amount of CH and decreasing amount of unhydrated clinker phases (C_2S and C_3S) with time were detected. LLi and HLi exhibited lower intensity of CH, C–S–H, and ettringite peaks than PC at the three testing ages with decreasing distinctions over time. At 7 days, a positive correlation between these peak intensities with lithium dosage was observed, while it converted to a reverse trend at 28 and 90 days. This is again due to the retarded later-age cement hydration in the presence of the increasing amount of lithium. Compared with PC, additional C–S–H, less CH, and fewer anhydrous clinker phases were detected from DMK, especially after 28 days. In line with the TGA data, the developments of both anhydrous phases and newly formed hydration products mainly occurred during the first 28 days, and less significant evolutions were detected thereafter. Alumina-rich hydrate phases, such as strätlingite, hydrogarnet, and zeolite can be identified from the groups containing MK, especially the ones with MIC. This is a result of the pozzolanic reactions between MK and cement hydration products [28,62]. While the amount of ettringite in the groups without MK increased over time up to 28 days, less ettringite was detected in the samples with MIC. No ettringite can be detected at 90 days from FMIC and FMIC-Li. In the MIC groups, fewer CH, C_2S, and C_3S, and more C–S–H and hydrogarnet phases were formed in the presence of MK with higher DOS, which again indicates the positive correlation between the cement hydration enhancement and the gradually released water as well as the enhanced pozzolanic reactions. Further evidence is the difference between FMIC and DMKEW: more C–S–H and hydrogarnet, and less CH formed in FMIC than in DMKEW. Different from TGA, the variation in CH in the presence of varying MK DOS is undetectable from XRD, which might be a result of the overlapped CH and strätlingite peaks at 34° 2θ. With the combined incorporation of lithium and fully saturated MK (FMIC-Li), the lowest C_2S and C_2S peaks, the highest zeolite peak, and the disappearance of the CH peak were obtained, which provides an indication of the desired synergistic effect between lithium and saturated MK in modifying phase evolution of the cement systems.

Fig. 9 presents the quantifications of the main phases in the pastes, such as anhydrates (C_2S/C_3S and gypsum), amorphous phase, CH, crystalline C-(A)-S-H, ettringite, hydrogarnet, zeolite, and strätlingite, based on the Rietveld refinement of the XRD data. The profile R-values of lower than 0.08 indicate a good fitting in the refinement analysis. It should be noted that the amorphous phases might also include some unhydrated cement and MK. It can be seen that the anhydrates phases decreased over time in all the groups, indicating the expected hydration process. In the presence of lithium, however, more anhydrates were observed than in PC after 90 days, revealing the retarding effect of lithium in cement hydration as discussed above. For the groups containing MK, the anhydrates decreased significantly over time. When 30% dry MK was incorporated, the anhydrates content decreased from 27.7% to 19.8%, while in the presence of MIC, the anhydrates content further decreased to 16.5% (0.5MIC), 15.7% (0.75MIC), and 13.8% (FMIC) after 90 days. It should be noted that the FMIC-Li group showed the lowest anhydrate content of 11.0% after 90 days, which is 15.9% lower than that of PC indicating a synergistic effect between saturated MK and lithium in enhancing the degree of cement hydration.

In this XRD refinement, both the amorphous phase and the crystalline chondrodite, suolunite, and tobermorite were quantified as C–S–H [63]. In PC, the content of the amorphous phase increased from 21.0% to 26.2% from 7 days to 90 days, and the crystalline C-(A)-S-H increased from 16.7% to 21.2%. Due to the retarded long-term cement hydration in the presence of lithium, 0.3% and 1.7% less crystalline C-(A)-S-H was formed in LLi and HLi, respectively. With the incorporation of MK, either in dry or saturated conditions, no significant difference in the amorphous phase was observed, while the content of crystalline C-(A)-S-H

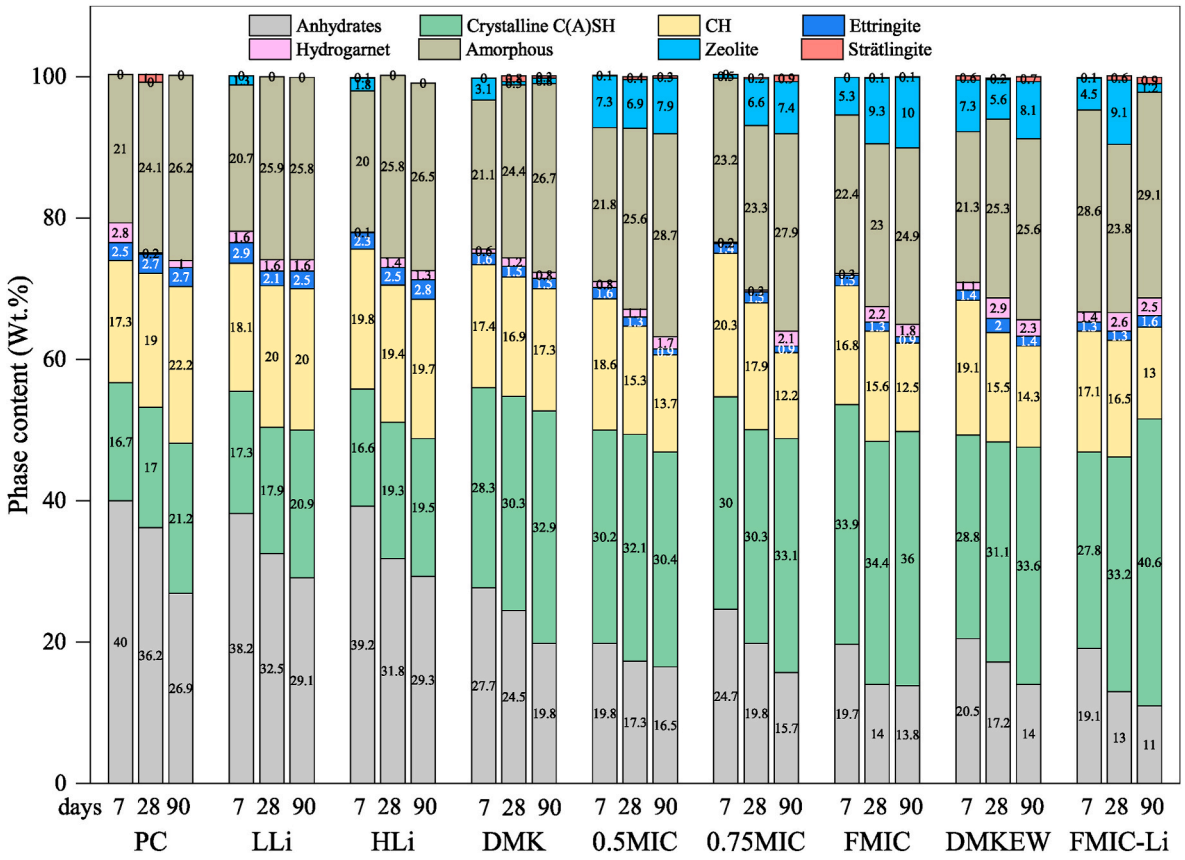

Fig. 9. Phase assemblage evolution quantified by XRD Rietveld refinement.

was increased. After 90 days, DMK showed an 11.0% higher crystalline C-(A)-S-H content than PC. Although 0.5MIC exhibited a lower crystalline C-(A)-S-H than DMK, it is still 9.2% higher than that of PC. At higher MK DOS of 75% and 100% (0.75MIC and FMIC), the crystalline C-(A)-S-H content was increased to 33.1% and 36.0% after 90 days, which are 11.9% and 14.8% higher than that of PC, respectively. Compared with the MIC groups, the direct addition of extra mixing water (DMKEW) resulted in a lower 90-day crystalline C-(A)-S-H content of 33.6% but a higher amorphous phase content of 25.6%. It is interesting to observe the synergistic effect between lithium and the saturated MK again in FMIC-Li, in which the highest crystalline C-(A)-S-H content of 40.6% was obtained.

Another main cement hydration product, CH, however, is normally considered the weak part in hardened cement paste as it can introduce initiation and growth of micro-cracks thereby negatively impacting the strength development of concrete [64]. In line with the TGA results, an increase in CH content over time was observed in PC showing a value of 22.2% after 90 days, which is 4.4% higher than the TGA data. Along with the decreased C-(A)-S-H content, 0.2% and 0.5% less CH was precipitated in LLi and HLi after 90 days. The development of CH in the groups with MK is a result of the dynamic tradeoff between the hydration enhancement (which produces more CH) and the pozzolanic reactions (which consume CH). It is interesting to note that, the 7-day CH contents of the cement-MK blends (either dry or saturated MK) are slightly higher than that of PC. This is, in particular, the case of DMKEW, which exhibited a 1.8% higher 7-day CH content than PC, indicating the enhanced early-age cement hydration reactions in the presence of MK particles and extra mixing water. In the later ages, however, the CH contents in these cement-MK groups became lower than that of PC, revealing the predominant lime consumption driven by pozzolanic reactions. It was worth noting that the amounts of CH determined by the XRD refinement are relatively higher than that from TGA. This might be due to the underestimation in TGA caused by the incomplete decomposition under the employed heating rate or the overestimation of CH in the Rietveld refinement analysis due to the unidentified phases in the samples, which was also identified in previous studies [65,66]. In line with the changes in CH content, less ettringite was formed in the presence of MK, while the groups containing saturated MK showed more hydragarnet and zeolite than the blends with dry MK and lithium, which might be due to the enhanced reaction of aluminate triggered by MIC. Although 30% cement was replaced by MK, only 0.1%–0.9% strätlingite was detected from the MIC groups, which might be due to the low reaction degree and the incomplete depletion of CH in the cement systems. Compared with FMIC, the coexisting of lithium and saturated MK resulted in further decreased contents of ettringite and zeolite, but more hydrogarnet.

3.3.3. ATR-FTIR analysis

Fig. 10 displays the ATR-FTIR spectra of the hydrated cement pastes after 7, 28, and 90 days. The evolutions of cement hydration products with time, such as the O–H stretching vibration from CH, the SO_4^{2-} vibration in ettringite, and the asymmetric Si–O stretching vibration in Q^2 tetrahedral of C–S–H phases at ~3640 cm^{-1}, ~1110 cm^{-1}, and ~960 cm^{-1} [67–69], respectively, were identified. In PC, both the CH and C–S–H peaks increased over time, and the span attributed to ettringite was kept almost constant for the entire testing period. In LLi and HLi, the peaks due to the vibrations of CH, C–S–H, and ettringite increased with the dosage of lithium at 7 days, but both of them became lower than that of PC after 28 days, which is in line with the calorimetry and TGA results and indicates the accelerating and retarding roles of lithium in early- and later-age cement hydration, respectively. The second agreement with the TGA and XRD results is the decreased ettringite peak over time indicating the accelerated conversion of AFt to AFm introduced by lithium. In the presence of dry MK, increased C–S–H peaks and

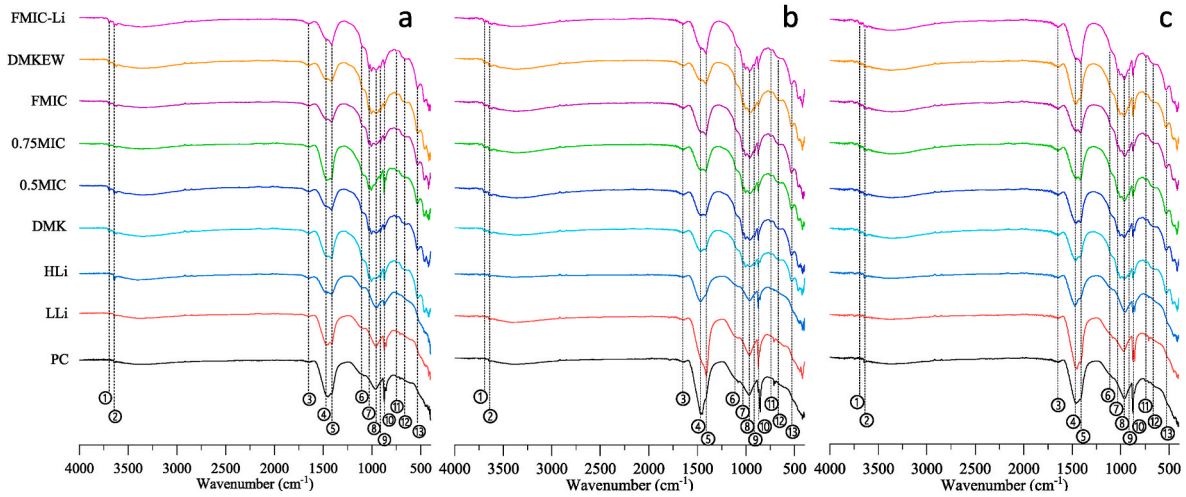

Fig. 10. ATR-FTIR spectra of the hydrated cement pastes at (a) 7 days, (b) 28 days, and (c) 90 days (1: 3694 cm^{-1}, 2: 3640 cm^{-1}, 3: 1650 cm^{-1}, 4: 1470 cm^{-1}, 5: 1415 cm^{-1}, 6: 1110 cm^{-1}, 7: 1032 cm^{-1}, 8: 960 cm^{-1}, 9: 918 cm^{-1}, 10: 873 cm^{-1}, 11: 745 cm^{-1}, 12: 670 cm^{-1}, 13: 533 cm^{-1}).

decreased CH peaks were detected, while in the cement blends containing saturated MK, the decrease in CH and increase in C–S–H phase were more significant indicating the enhanced hydration and pozzolanic reaction. The comparison between DMKEW and FMIC again confirms the superior role of gradually released water from the saturated MK to mixing water in sustaining pozzolanic reactions to consume CH and form additional C–S–H. In addition, due to the accelerated phase conversion, the peak of ettringite disappeared in the presence of fully saturated MK (FMIC) and the coupled incorporation of lithium and saturated MK (FMIC-Li).

The signals at ~670 cm^{-1} and ~1005 cm^{-1} indicate the existence of C-A-S-H [70], while the multiple peaks in the range between 420 cm^{-1} to 534 cm^{-1} are contributed to the O–Si–O or O–Al–O bending vibration in C-A-S-H and AFm phases [71]. Compared with PC, LLi, and HLi, additional peaks attributed to C-A-S-H, which increased with DOS of MK, were observed in the groups containing MK. A pronounced increase of the C-A-S-H peaks was detected from FMIC-Li, indicating the coupling effect of lithium and saturated MK in the formation of hydrates with enhanced incorporation of aluminum. Due to the carbonation of CH and C–S–H, the peaks at ~1415 cm^{-1}, ~1470 cm^{-1}, ~873 cm^{-1}, ~745 cm^{-1}, and ~714 cm^{-1} attributed to the bending or stretching vibrations of $[CO_3]^{2-}$ in calcite, aragonite, and vaterite [67,72] were observed. It is interesting to observe that decreased peaks of carbonates were observed in the groups with lithium and saturated MK after 7 days, which might be due to the less available CH in these groups. O–H stretching and bending vibrations in the interlayer and capillary water molecules were detected at ~3397 cm^{-1} and ~1650 cm^{-1} [73]. Increasing water contents positively correlated to the DOS of MK was detected from MIC groups to continuously fuel the hydration of cement. Moreover, characteristic peaks of kaoline at ~3694 cm^{-1}, 1032 cm^{-1}, and 918 cm^{-1} [74] due to the unreacted MK were observed in the groups containing MK. Although decreased over time, these peaks can still be detected from DMK even after 90 days revealing the low DOR_{MK}. By saturating MK, these peaks disappeared in FMIC after 28 days, which agrees with the TGA findings that the DOR_{MK} can be effectively improved when it is incorporated as saturated particles. The synergistic effect of lithium and saturated MK in pozzolanic reactions was again confirmed by the detected highest DOR_{MK} from FMIC-Li.

3.3.4. ^{29}Si and ^{27}Al MAS NMR studies

Fig. 11a shows the ^{29}Si MAS NMR spectra and the corresponding optimized deconvolutions of selected pastes after 650 days of hydration. In line with the TGA analysis, anhydrates in terms of Q^0 sites in alite (−60 and −65 ppm) and belite (−71.5 ppm) were detected in PC, indicating the low DOH of cement. In the presence of lithium (HLi), the Q^0 peaks exhibited higher intensity than in PC, especially the one for belite (−71.5 ppm), indicating retarded hydration of cement. In light of the calorimetry data and the development of DOH of cement in the presence of lithium above, the fast reaction between lithium and cement during the first day might result in the precipitation of inhomogeneous lithium-incorporated products as a coating on the surface of belite particles [75], which retarded the continuous reaction of belite. However, with the incorporation of MK, the Q^0 peaks decreased, which positively correlated to the DOS of MK. FMIC and FMIC-Li showed the lowest anhydrate signals, which again indicates the benefits of MIC in enhancing cement hydration. Different from the dominant resonance of Q^1 sites (−76 to −82 ppm) in C–S–H of PC, Q^2 site in the range of −82 ppm to −88 ppm dominated the spectra of MK groups, which indicates the enhanced formation of middle/bridge SiO_4 tetrahedra in C–S–H. A new $Q^3(1Al)$ peak at around −94 ppm appeared in MK groups, revealing the incorporation of Al in C–S–H (C-A-S-H gels).

After 650 days of hydration, the SU, AT, and MCL of PC exhibited the same value of 3.0, indicating the ignorable incorporation of Al in C–S–H as evidenced by the low $R_{Al/Si}$ of 0.0008. The three chain length values increased to 3.2 in the presence of lithium (HLi) along with a slight increase of $R_{Al/Si}$ to 0.003 indicating the increased polymerization (PD increased from 0.5 to 0.6). However, HD decreased from 0.6 to 0.5 confirming the retarded cement hydration in the presence of lithium. By replacing 30% of cement with dry MK, 13.3% decrease in SU and 53.3% increase in AT were observed, indicating the incorporation of Al into C–S–H. This was verified by the 10.4%, 23.3%, and 349% increases in PD, HD, and $R_{Al/Si}$, respectively. As a result, MCL was elongated by 3.3% in comparison with that of PC. The comparison between the cement blends containing dry and saturated MK again confirmed the benefits of MIC in promoting cement hydration and pozzolanic reactions. In 0.5MIC, the values of SU, AT, MCL, PD, HD, and $R_{Al/Si}$ are 3.9%, 15.2%, 0.6%, 5.7%, 1.4%, and 14.3% higher than that of DMK, respectively. In FMIC, the six values were all further increased, indicating the more pronounced enhancement in cement hydration and the formation of more and longer C-A-S-H chains with more Al incorporated into C–S–H. More interestingly, the synergistic effect of lithium and saturated MK was again confirmed by the further increased values in these molecular-scale results except for HD. AT and PD values are 6.3% and 4.5% higher than that of FMIC, and 126.7% and 91.7% higher than that of PC, respectively, which support the TGA, XRD, and FTIR findings.

Fig. 12a shows the ^{27}Al MAS NMR spectra and the optimized deconvolutions of the paste samples, in which the intensities of peaks related to Al sites in specific phases were identified. Consistent with the

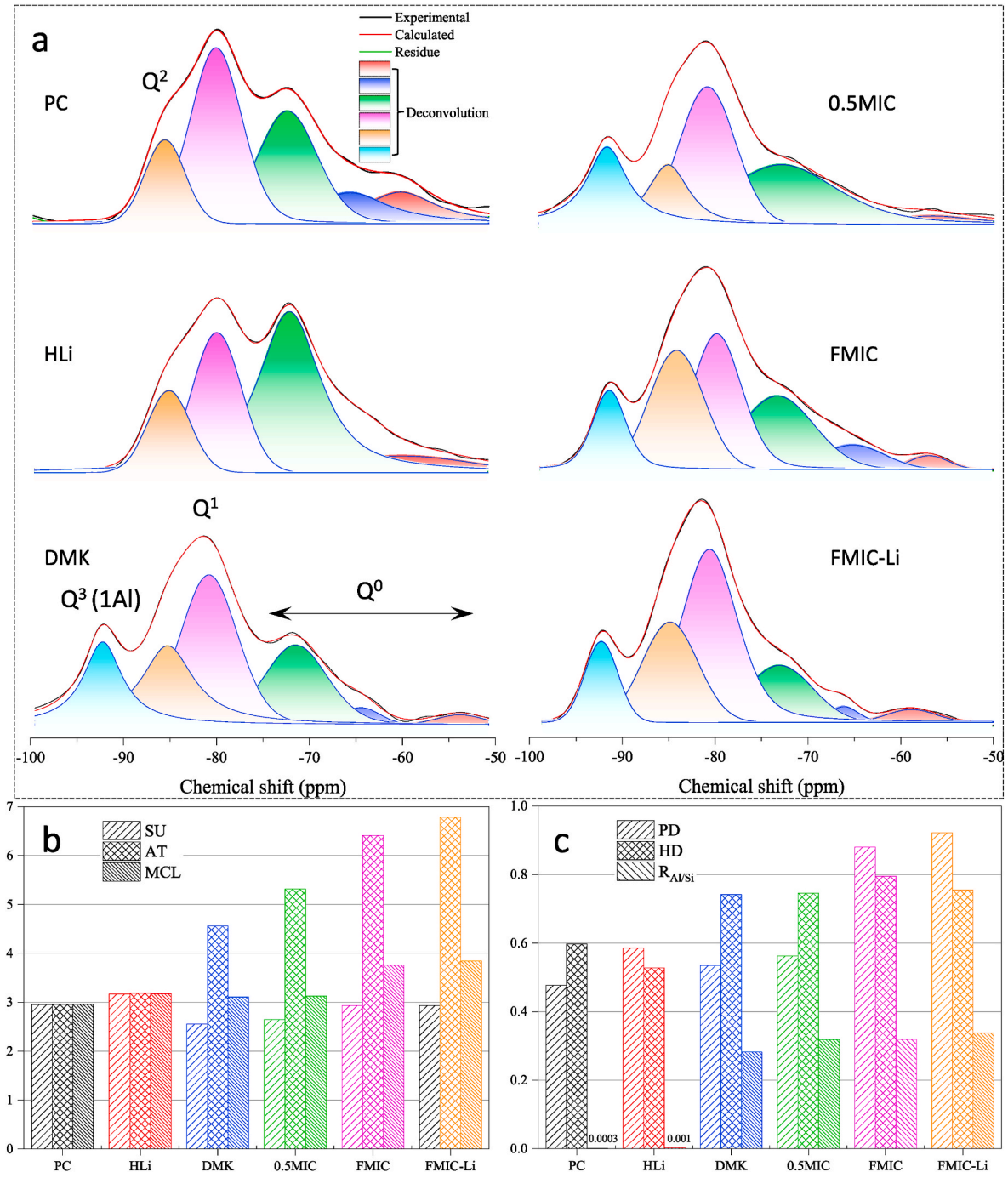

Fig. 11. (a) ^{29}Si MAS NMR spectra and corresponding optimized deconvolutions of PC and cement blends after 650 days, (b) average silicate chain lengths, aluminosilicate chain lengths, mean molecular chain length of the C–S–H phases, and (c) polymerization degree, hydration degree, the average Al/Si molar ratio in the chains of tetrahedra.

^{29}Si NMR results, HLi exhibited higher intensity of anhydrates (belite (~79.6 ppm) and alite (~88.7 ppm)) than PC. More specifically, a slight increase in the alite peak and remarkable enhancement in the belite peak were observed. This again confirmed the observations from ^{29}Si NMR above that lithium can retard the hydration of belite more significantly than that of alite at later ages. This might be due to the fact that alite possesses a higher reaction rate and a higher DOR than belite and hence less impact from lithium at this stage. However, these anhydrates were not detected in the groups containing MK. These two contrasts verify the TGA and XRD findings in the different roles of lithium and MK in modifying cement hydration. The conversion of ettringite to AFm in PC can be identified from the different peak intensities at 10.6 and 13.9 ppm, which agrees with the NMR findings in Ref. [28]. However, in HLi, the conversion of ettringite into AFm was mitigated. According to Coumes et al. [76], lithium can promote the initial precipitation of AFm and its later conversion into AFt phases. Interestingly, the ^{29}Al NMR spectra of the pastes containing MK are dominated by AFm and the peak of ettringite turned into a minor shoulder. This supports the enhanced AFm formation as found in the TGA results.

It is interesting to see that, in the presence of lithium, the incorporation of Al into the C–S–H chains was improved resulting in higher intensity of C-A-S-H phases (36.2 and 74.0 ppm) than in PC. This might

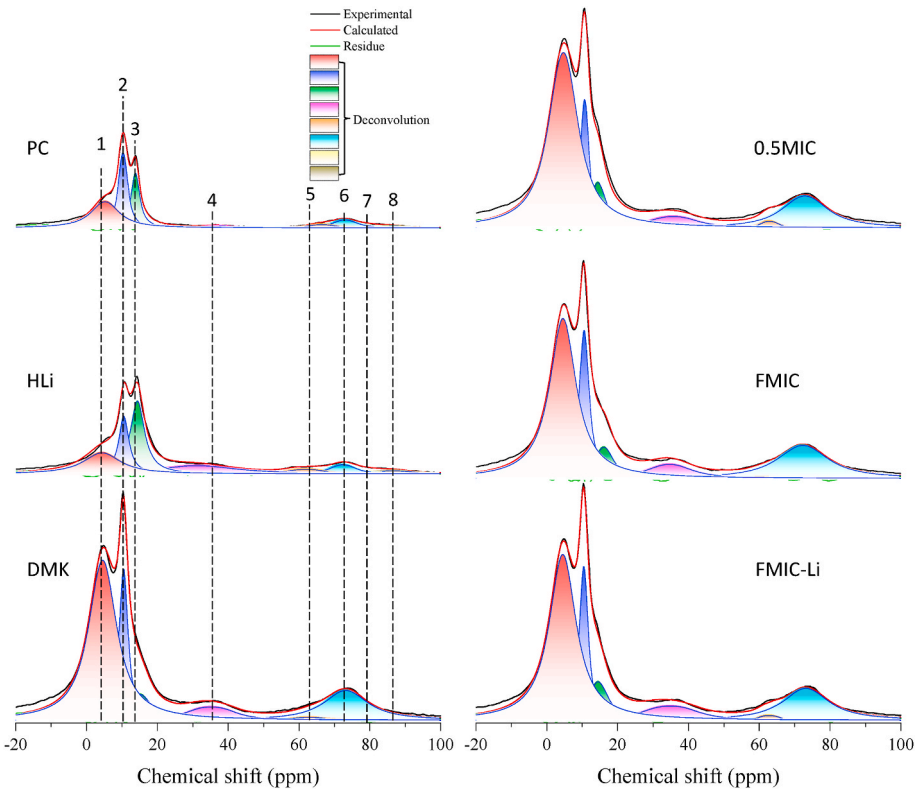

Fig. 12. ^{27}Al MAS NMR spectra and corresponding optimized deconvolutions of hydrated PC and cement blends after 650 days (1: Al(VI)/TAH; 2: AFm; 3: Ettringite; 4/6: C-A-S-H; 5: strätlingite; 7: Belite; 8: Alite).

be due to the promoted dissolution of aluminate induced by lithium to form Li-containing amorphous $Al(OH)_3$ [77], which accelerates the absorption of aluminum into C–S–H. This enhancement is more pronounced in the MK-modified cement pastes triggered by the introduced Al from MK. Compared with dry MK, saturated MK and the coupling incorporation of lithium and saturated MK further improved the formation of C-A-S-H. This is in line with the ATR-FTIR findings. In addition to AFm and C-A-S-H, significant intensity increases were observed in the MK groups for a peak at 4.5 ppm, which might be due to the silicate-bridging Al(VI) ($[AlO_2(OH)_4]^{5-}$) sites in C-A-S-H [78]or hydrogarnet [79], or the formation of "third aluminate hydrate" (TAH) phase on the surface of C–S–H [80]. It is again interesting to see the further improvement of this third Al-related phase evolution triggered by the saturated MK and the coexistence of saturated MK and lithium over dry MK, which is consistent with the development of hydrogarnet obtained from XRD.

3.4. Thermodynamic modeling

The evolutions of the hydrate phases of PC, DMK, 0.5MIC, and FMIC calculated through thermodynamic modeling based on the observed dissolution and DOR of the anhydrous phases are shown in Fig. 13. The compositions of the phase assemblage (mass g per 100g of cement) were calculated as a function of hydration time based on the DOH_{PC} and DOR_{MK} acquired from the TGA analysis. According to reaction kinetics, goethite and hematite can only precipitate at elevated temperatures, such as 50 °C within months or 80 °C within days [81], and gibbsite forms at temperatures above 60 °C [82], while the formation of thaumasite needs a temperature below 10 °C [83]. Therefore, in this thermodynamic modeling, these minerals were excluded from the outputs. Fig. 13a shows the phase assemblage of PC up to 90 days, where the formation of C–S–H, portlandite, ettringite, and Fe–Al-containing siliceous hydrogarnet ($C_3(AF)S_{0.84}H$) were predicted. From the TGA data, the DOH of cement in PC experienced a rapid increase during the first 28 days reaching a value of 73.0%, while a significantly less increment was observed from 28 days to 90 days. In the thermodynamic modeling, for each 100 g of binder, 27.6 g of C–S–H and 7.9 g of ettringite were formed in PC after 1 day, which increased to 46.5 g and 13.3 g, respectively, after 28 days. However, the contents of C–S–H and ettringite only increased by 0.04 g/100 g binder and 0.01 g/100 g binder, respectively, from 28 days to 90 days. A CH (portlandite) content of 14.4 g/100 g binder was predicted after 1 day, which is consistent with the value obtained from TGA. After 28 days, the thermodynamic modeling yielded a portlandite content of 24.4 g/100 g binder, which is 6.9% higher than the TGA results. This discrepancy might be due to the overestimated DOH_{PC} based on the proposed calculation method in Eq. (7).

Fig. 13b–d presents the phase assemblages of DMK, 0.5MIC, and FMIC. Interestingly, compared with PC, Mg–Al hydroxycarbonate (OH-hydrotalcite) was formed in the presence of MK with a positive correlation with MK DOS. After 90 days, DMK, 0.5MIC, and FMIC yielded 5.5 g, 5.9 g, and 6.5 g OH-hydrotalcite per 100 g binder, respectively. The increased DOH of cement due to MIC and the high aluminum content in MK are critical in resulting in this phenomenon. The second result of the enhanced cement hydration and pozzolanic reactions is the complete consumption of portlandite. Therefore, compared with PC, additional C-(A)-S-H and hydrogarnet, and less ettringite were formed in the three blended cement pastes. With the complete consumption of portlandite, the preferential reaction between the amorphous aluminate from MK and portlandite to form calcium aluminate hydrates (hydrogarnet) was eliminated, which triggered the reaction between belite (C_2S) and Al $(OH)_3$ for the precipitation of strätlingite [84,85]. 0.5MIC and FMIC showed decreasing amounts of MK with time revealing the enhanced dissolution of MK and improved pozzolanic reactions in the cement systems induced by MIC. The improved DOR of MK (DOR_{MK}) in 0.5MIC and FMIC provided additional Al ($Al_2O_3^{5-}$) [86] triggering the precipitation of ettringite. Compared with PC and DMK, the contents of C-(A)-S-H, hydrogarnet, and strätlingite were further improved in the two groups with MIC and, again, a positive correlation with MK DOS was

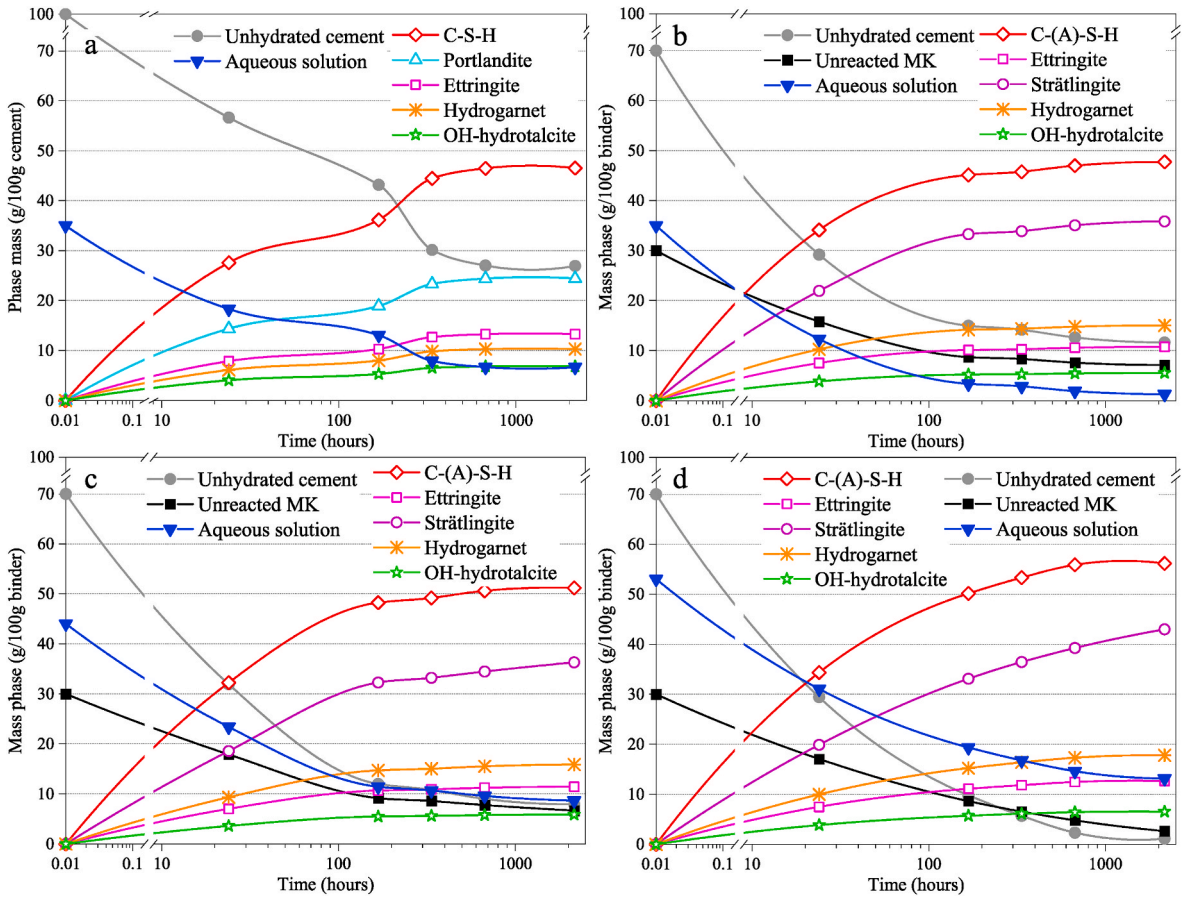

Fig. 13. Phase assemblages of (a) PC, (b) DMK, (c) 0.5MIC, and (d) FMIC predicted via thermodynamic modeling.

observed. The 7-day C–S–H content increased from 45.1 g to 48.2 g and 50.1g per 100 g binder by increasing the MK DOS from 0 to 50% and 100%, respectively. A more significant increase of C–S–H from 14 days to 90 days was obtained in the presence of MK with higher DOS suggesting the effective role of saturated MK in sustaining long-term cement hydration and phase evolution. After 90 days, compared with DMK, 0.9% and 2.8% more hydrogarnet and 1.4% and 20.0% more strätlingite were formed in 0.5MIC and FMIC, respectively. The precipitations of C-(A)-S-H and Al-rich hydrate phases confirm the experimentally detected positive role of saturated MK surpassing the conventional direct incorporation of dry MK in optimizing cement hydration. It should be noted that, in the thermodynamic analysis, the water for MK's saturation was inputted as a part of mixing water, which only increases the w/b ratios of the systems (hence more pore solutions in Fig. 13c and d) and the favorable gradual release of water in saturated MK cannot be fully launched. Based on the experimental comparison between FMIC and DMKEW in TGA and XRD, the gradually released water from the saturated MK outperforms the extra free water in modifying cement hydration suggesting that the role of the saturated MK might be underestimated in this thermodynamic simulation.

To further uncover the role of saturated MK in modifying the phase evolution in hydrated cement at varying DOR of MK (DOR_{MK}), Fig. 14a and b shows the phase assemblage as a function of DOR_{MK} in DMK and FMIC, respectively, at an assumed constant DOH of cement (DOH_{PC}) of 80%. It is seen that when MK's reaction degree is lower than 21%, the hydration products are mainly constitutive of C–S–H, portlandite, ettringite, hydrogarnet, monosulfate (AFm), OH-hydrotalcite, and unreacted MK. When the DOR of MK exceeds 30%, both ettringite and portlandite disappear accompanied by an increased amount of monosulfate and C–S–H, as well as newly precipitated strätlingite. This is

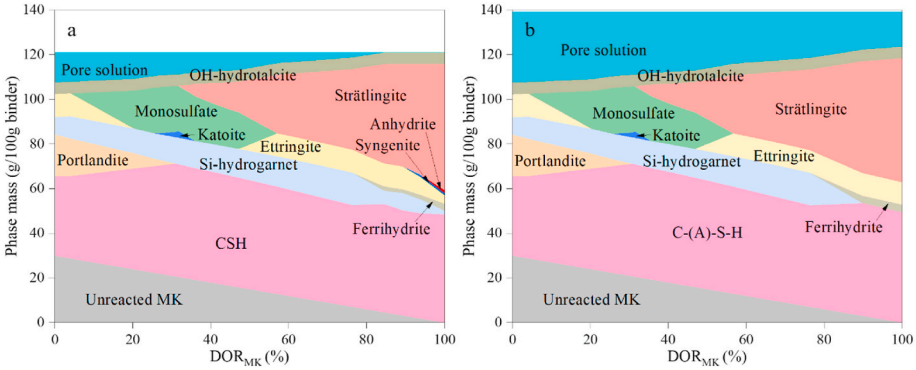

Fig. 14. Thermodynamic modeling of (a) DMK and (b) FMIC with varying DOR of MK and a constant DOH of cement at 80%.

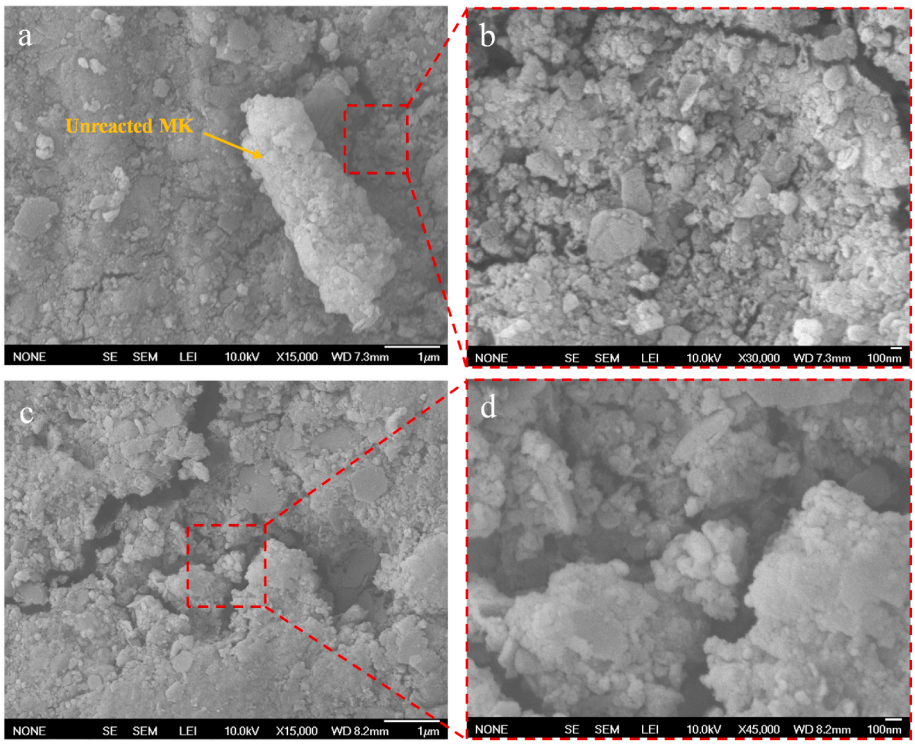

Fig. 15. SEM images of the cement pastes after 100 days: (a, b) DMK, and (c, d) FMIC.

consistent with the observations from the calorimetry studies above, as the ettringite could be converted to monosulfate during the first day of hydration when the cement is partially replaced with MK and the DOR_{MK} is low. A similar finding was also observed by Gijbels et al. [87]. The previous studies [7,88] reported that in the cement containing 15%–30% MK, the formation of strätlingite can be observed at 14 days and its content increased with ongoing hydration. This is in line with the current study that the amount of strätlingite increased with MK's DOR (DOR_{MK}). Monosulfate and katoite can only precipitate when DOR_{MK} is in the ranges of 4%–57% and 26%–35%, respectively. Therefore, these two phases were not predicted in the phase assemblages in Fig. 15, where the calculated DOH_{PC} and DOR_{MK} increasing rapidly with time were used. When the DOR_{MK} exceeds 47%, monosulfate starts converting back into ettringite, therefore the precipitation of ettringite was obtained again. This agrees with the previous observation by Liu et al. [89], where the sulfate ions from gypsum reacted with monosulfate to form ettringite. A complete conversion of monosulfate into ettringite occurred at DOR_{MK} of 57% in both cases. The hydrogarnet shows a gradual increase until the DOR_{MK} reaches 76%, from where this phase starts decreasing along with an increasing amount of C–S–H, strätlingite, and ferrihydrite. When DOR_{MK} exceeds 90%, hydrogarnet is completely dissolved in FMIC.

It is observed that the C-(A)-S-H content increases from 35.6 g/100 g binder to 50.5 g/100 g binder when the DOR_{MK} increases from 0 to 30%. With more MK reacted, less C-(A)-S-H precipitates in the cement systems, which might be due to the formation of Al-bearing products (i.e., hydrogarnet, strätlingite). At an ideal condition with 100% DOR_{MK}, 48.5 g and 49.4 g of C–S–H per 100 g binders can be formed in DMK and FMIC, respectively. In the meanwhile, DMK yielded 0.9% more strätlingite and 6.2% less ettringite than FMIC. This might be attributed to a higher sulfate ion diffusion from gypsum to monosulfate in the presence of an additional aqueous phase in FMIC, while the pore solution DMK is depleted when DOR_{MK} exceeds 90%. Due to the same reason, syngenite ($K_2Ca(SO_4)_2{\cdot}H_2O$) and anhydrite ($CaSO_4$) are oversaturated and precipitated [90] in DMK.

3.5. Micro-morphology analysis

SEM microscopic examination of DMK, 0.5MIC, FMIC, and FMIC-Li after 100 days of hydration was conducted to further uncover the influence of MIC and the coupling effect of lithium and MIC on the microstructure and distributions of the key hydration phases. By substituting 30% cement with MK with varying DOS, fewer portlandite sheets and needle-shaped ettringite can be detected in the pastes with MIC. Similar to lithium, controversy about the role of MK in the conversion of ettringite also exists. On the one hand, the formation of ettringite was found to be stimulated and enhanced by the Al from MK [91,92], and the transformation of ettringite to monosulfate can be retarded [93]. However, some studies found that, in the presence of MK, the conversion of ettringite into monosulfate can be enhanced [80,94,95], which is consistent with the experimental and thermodynamic modeling observations in this study. As shown in Fig. 15a and b, a dense mixture can be obtained in DMK. However, even after 100 days of hydration, unreacted MK particles can still be observed indicating the low DOR of this calcined clay mineral in the matrix of cement at a 30% substitution level. The high water absorption of dry MK and the use of a low w/b ratio (0.35), which worked together to limit the water for cement hydration and pozzolanic reactions, might be the main reasons. By incorporating saturated MK, more water can be provided from the adjacent MK particles to fuel the continuous cement hydration and pozzolanic reactions. As a result, as shown in Fig. 15c and d, fewer CH and ettringite, and additional gel-like C-(A)-S-H can be observed from FMIC.

In addition to the regular cement hydration products, a cubic phase was observed in the cement pastes with MIC. As shown in Fig. 16a, the massive precipitation of C–S–H gel with a limited amount of CH sheets was observed in 0.5MIC. A cubic phase with an average side length of 400–600 nm and a porous surface was formed. With the increased DOS of MK, in addition to the fewer CH sheets and additional C–S–H gels, the cubic phase was turned into well-crystallized cubes with less porous structure and a smaller size (side length of 200–500 nm) in FMIC (see Fig. 16b). In FMIC-Li, as shown in Fig. 16c and d, no cubic crystals can be

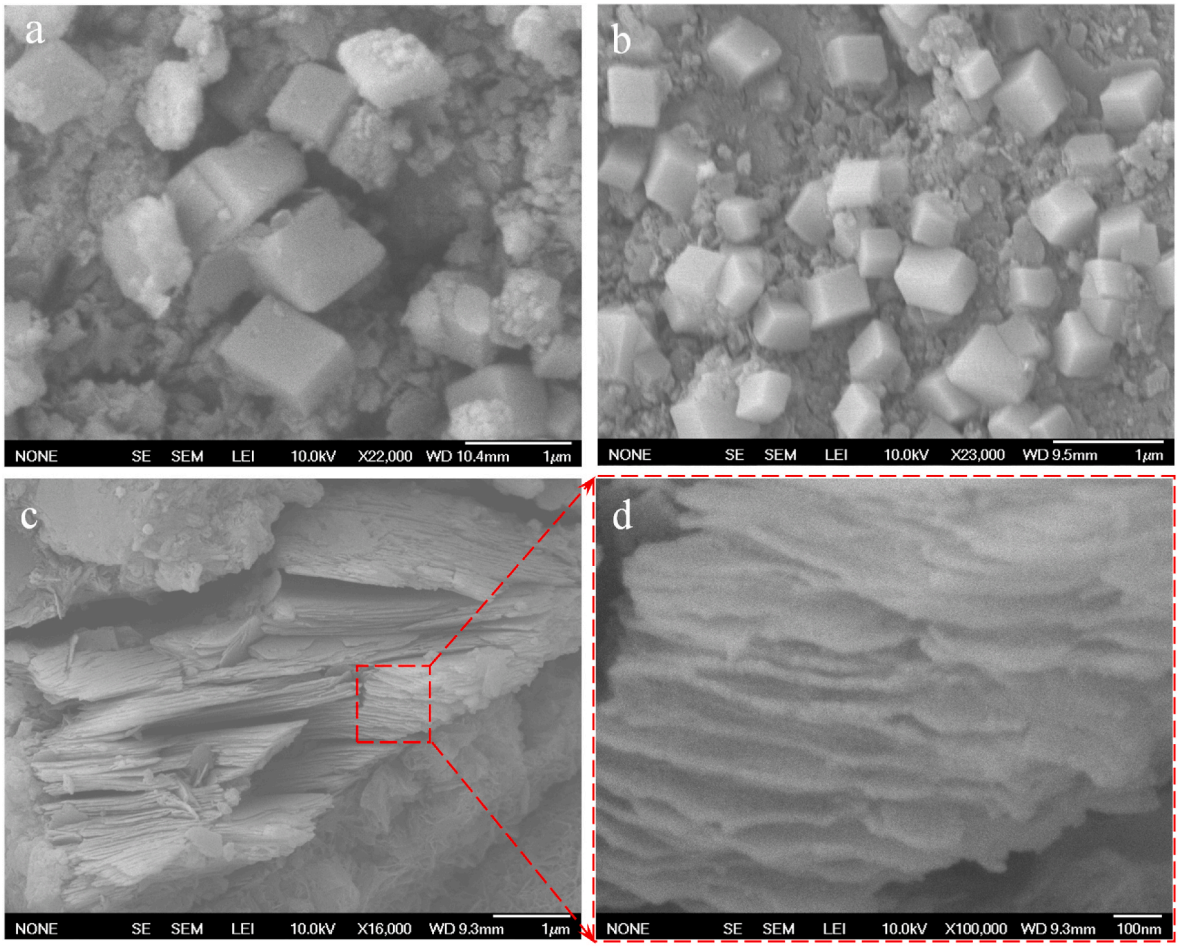

Fig. 16. SEM images of the cement pastes after 100 days (a) 0.5MIC, (b) FMIC, and (c, d) FMIC-Li.

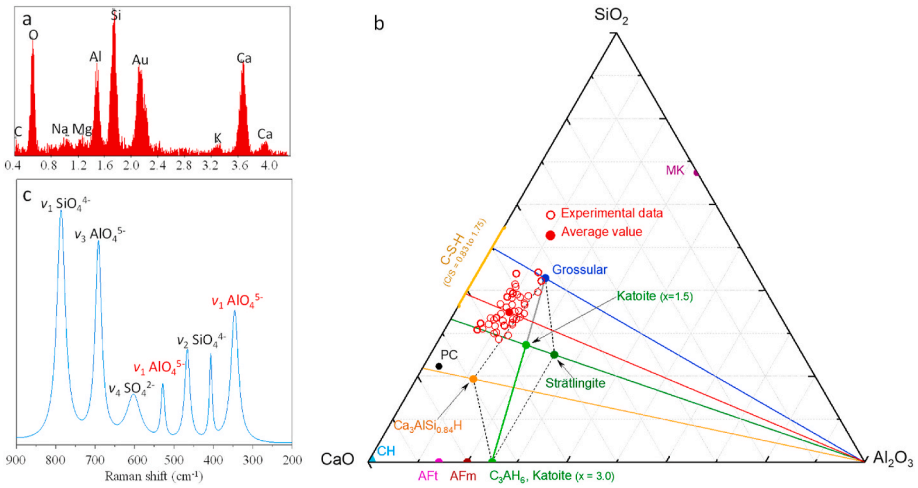

Fig. 17. (a) Representative EDX pattern, (b) comparison of experimental data of the cubic siliceous hydrogarnet and theory compositions of cement hydrate phases (molar fractions) in the $CaO–Al_2O_3–SiO_2$ ternary diagram, and (c) Raman spectrum of the cubic siliceous hydrogarnet in FMIC.

detected. Instead, a dense phase with a parallelly layered structure, which exhibits an interlayer space of 20–50 nm and an average layer thickness of 20 nm, was observed. According to Ref. [96], this layered phase might be C-(A)-S-H gel with interlayered Ca^{2+} cations, alkalis, water of hydration, as well as partial substitution of silicon with aluminum, which can be facilitated by the enhanced dissolution of MK in the matrix of FMIC-Li.

One probable explanation for the cubic phase is zeolite (chabazite) [97], which usually exhibits rhombohedral-shaped crystals that are pseudo-cubic. Previous studies have reported the formation of cubic zeolite in cementitious systems containing a variety of pozzolans, such as fly ash [98], bentonite [99], and MK [100], through either hydrothermal treatment [101] or alkali activation [102]. Under hydrothermal treatment, crystalline zeolite can be formed via a polymerization and depolymerization process, where the (Si, Al)–*O*-(Al, Si) bonds of pozzolans can be broken and rearranged in a heated aqueous solution (>100 °C) [103]. The alkali activation of pozzolans in cement binders is considered another process to trigger zeolitization, which starts with the dissolution of silica and alumina from pozzolans in the presence of alkali attacks, followed by the orientation of the dissolved species and the subsequent polycondensation reaction to form zeolite [104]. Although zeolite was detected by XRD (Fig. 8), this phase was not predicted by thermodynamic modeling with the database of CEMDATA18.1. Calcite from carbonation might be another possibility for the cubic phase, but noteworthy that the calcite crystal normally presents sharp edges [105] and carbonation has been minimized during the sample preparation.

Similar observations were obtained in blended cement or MK-lime matrix [106,107], where the cubic phase was considered non-siliceous hydrogarnet ($Ca_3Al_2(OH)_{12}$ or C_3AH_6), the precipitation of which was detected from the XRD and ATR-FTIR spectra (see Figs. 8–10) and predicted by the thermodynamic modeling (Fig. 14) in this study. Both the experimental and modeling results indicate that the incorporation of MK substantially increased the precipitation of this Al-rich phase, which further increases with the increasing DOS of MK in the MIC groups. Barbhuiya et al. [21] proposed that such cubic crystals in the hydrated cement paste containing MK are contributed to the transformation of calcium sulphoaluminate (ettringite) into calcium aluminate hydrates. When referring to phase stability, this hydraulic stable cubic phase can also be obtained from the conversion of strätlingite and tetracalcium aluminate hydrate (C_4AH_{13}) in lime–MK pastes at higher curing temperatures and longer curing ages [108].

Based on the element ratios of the cubic phase determined by EDX (see a representative spectrum in Fig. 17a) and their locations in the $CaO–Al_2O_3–SiO_3$ phase diagram (Fig. 17b), the possibilities of zeolite and calcite were excluded. The cubic phase exhibited an average Ca/Si ratio of 3.08, which is between grossular and katoite (x = 1.5, i.e., $Ca_3Al_2(SiO_{12})_{1.5}(OH)_6$) (or strätlingite). The average Si/Al ratio is about 2.22, which indicates that, compared with zeolite and non-siliceous hydrogarnet, the detected cubic phase is more likely to be siliceous hydrogarnet, a solid solution with end members of grossular ($Ca_3Al_2(SiO_4)_3$) and katoite ($Ca_3Al_2(SiO_{12})_{3-x}(OH)_{4x}$, $x = 1.5$ to 3.0). It is noted that the content of silica of the detected siliceous hydrogarnet is higher than that of $Ca_3(Al, Fe)Si_{0.84}H$ and the content of aluminum is lower than that of the grossular-katoite solid solution, which might be due to three probable reasons: (i) substitution of Al by Fe that promotes the phase stabilization [109], (ii) increased dissolution of silica in pore solution induced by the improved DOH of cement and DOR of MK; and (iii) residual C-(A)-S-H on the surface of the cubic phase that causes EDX deviation. The Raman spectrum of FMIC shown in Fig. 17c confirmed the formation of hydrogarnet, in which stretching vibrations of the v_1 AlO_4^{5-} from hydrogarnet were observed at 345 cm^{-1} and 527 cm^{-1} [110, 111] along with the symmetric stretching vibration of v_3 AlO_4^{5-} (691 cm^{-1}) and v_1 SiO_4^{4-} (787 cm^{-1}) in C-A-S-H [55,112], the vibration of v_4 SO_4^{2-} (604 cm^{-1}) in brownmillerite, and the vibration of v_2 SiO_4^{2-} (466 and 406 cm^{-1}) in C–S–H.

In general, in a system of $CaO–Al_2O_3–H_2O$, non-siliceous hydrogarnet is considered the most stable phase, and the metastable calcium aluminate hydrates (e.g. CAH_{10} and C_2AH_8) eventually convert into this phase under ambient temperature [113,114]. In the presence of dissolved silicate species in pore solution, the formation of siliceous hydrogarnet can be triggered to further enhance phase stabilization with significantly reduced solubility [115]. Although the kinetics and mechanisms remain unclear, silicious hydrogarnet has been thought to be the stable phase of AFm [116]. Many previous studies identified that, different from other Si or Al-bearing phases, the formation of siliceous hydrogarnet can only be triggered at elevated temperatures in a $CaO–Al_2O_3–SiO_2–H_2O$ system or after an extremely long age (>20 years) in hydrated cement systems [109,117,118] indicating the low rate and difficulty of silicon incorporation in the stable hydrogarnet phase. This slow kinetic might be due to the extremely low concentrations of dissolved silica in the pore solution of PC or even DMK and the consequent unsaturation or low oversaturation of siliceous hydrogarnet in the

presence of AFm [109,119]. In the cement matrix with MIC, the enhanced cement DOH and MK DOR provide additional dissolved alumina and silica, which might be a trigger for the incorporation of silicon in hydrogarnet. As shown in the thermodynamic modeling, AFm disappears in the cement paste with MIC when the DOR of MK is over 56%, which might promote the oversaturation and precipitation of siliceous hydrogarnet. The formation of the well-crystallized siliceous hydrogarnet cubes in the MIC groups at ambient temperature paves a new way for precise control of target reaction products in the cement system without less dependence on extreme experimental conditions. More insights into this area will be gained in the authors' future research.

4. Conclusions

In this study, the roles of saturated MK, lithium, and their combined effects on hydration and phase evolution of cement, as well as the development of morphology and molecular structure of the hydration products were investigated. The primary insights and conclusions drawn from this work include.

1. Accelerated cement hydration during the first 24 h and the retarded hydration after 1 day in the presence of lithium is confirmed. From the NMR results, lithium mainly retards the hydration of belite in the later ages. From the calorimetry analysis, an increased cumulative heat evolves during the early hydration in the presence of MK indicating enhanced cement hydration. The saturated MK results in further cement hydration enhancement with more cumulative heat release. Along with the accelerated silicate reaction, renewed C_3A dissolution forming ettringite and its subsequent conversion into monosulfate are enhanced.
2. A substantial decrease in CH content in the presence of 30% dry MK is obtained, while the incorporation of saturated MK results in higher non-evaporable water content and degree of cement hydration. The desired coupling effect of lithium and saturated MK in enhancing cement hydration results in the highest DOH of cement among all the groups.
3. The formation of aluminum-containing phases strätlingite, hydrogarnet, and zeolite, low contents of CH and ettringite, as well as more C-(A)-S-H phases detected from TGA, XRD, ATR-FTIR, and ^{27}Al NMR provide experimental evidence of the effective role of saturated MK in enhancing cement hydration and phase evolution.
4. The synergistic effect between lithium and saturated MK on pozzolanic reactions is confirmed by the detected highest DOR of MK from FMIC-Li. ^{29}Si NMR results identify the modification of the C–S–H structure by saturated MK, such as the increased aluminosilicate chains, which are correlated to the higher $R_{Al/Si}$. The ^{27}Al NMR results reveal that lithium can promote the dissolution of aluminate and its incorporation into C–S–H gels. Combined with the introduced Al from MK, further increases in chain length of aluminosilicate tetrahedra, polymerization degree, and precipitation of Al-rich phases are observed from the paste containing coupled saturated MK and lithium.
5. The controversial roles of lithium and MK in the formation and conversion of ettringite are clarified. Inhibition of ettringite formation in the presence of lithium and enhancement of ettringite conversion induced by MK, although not considerable, are confirmed by both the experimental and modeling characterizations.
6. The phase assemblages of thermodynamic modeling well support the experimental observations of portlandite depletion, ettringite conversion, formations of additional C-(A)-S-H, hydrogarnet, and strätlingite. At 90 days, compared with the cement pastes containing dry MK particles, dissolution of 19.6% more MK and precipitations of 17.6% more C-(A)-S-H and 20.0% more strätlingite are triggered by the saturated MK.
7. The micro-morphology analysis confirms the formation of the denser mixture and inhibited precipitation of ettringite in the presence of MIC, and in particular, the formation of the cubic siliceous hydrogarnet, which evolutes to smaller and better crystalline cubes in the presence of MK with higher DOS. This phase might be induced by the raised dissolution of aluminum and silicate due to the enhanced DOH of cement and DOR of MK in the presence of saturated MK.

In summary, compared with the conventional use of dry MK, saturated MK, and in particular, its coexistence with lithium, showed superior performance in enhancing the dissolution of MK and hydration of cement, forming stable Al-rich phases, promoting the incorporation of Al in the silicate chain and modifying the molecular structures of C-(A)-S-H.

Declaration of competing interest

The authors declare that they have no known competing financial interests or personal relationships that could have appeared to influence the work reported in this paper.

Data availability

Data will be made available on request.

Acknowledgment

This study was supported by the United States National Science Foundation (NSF) [Award No. 1935799]. The authors gratefully acknowledge the support from this funding and thank Mr. Gary Howe and Dr. Earl Ada at the University of Massachusetts Lowell for their assistance with laboratory tests.

Appendix A. Additional TGA and DTG curves

The TGA and DTG curves of the hydrated cement admixtures at 7, 14 and 28 days are shown in Fig. A.1. It presents that the evaporable water of all the groups decreased significantly from 28 days to 90 days. Comparing with the short-term hydration, the intensities of the entherdomic peaks due to the decomposition of ettringite from all the groups decreased at later ages. In comparison, the more significant decreases of ettringite in the groups containing MK were probably due to the pozzolanic reactions and the enhanced conversion of AFt to AFm as accompanying increased AFm decompositions were observed from these groups.

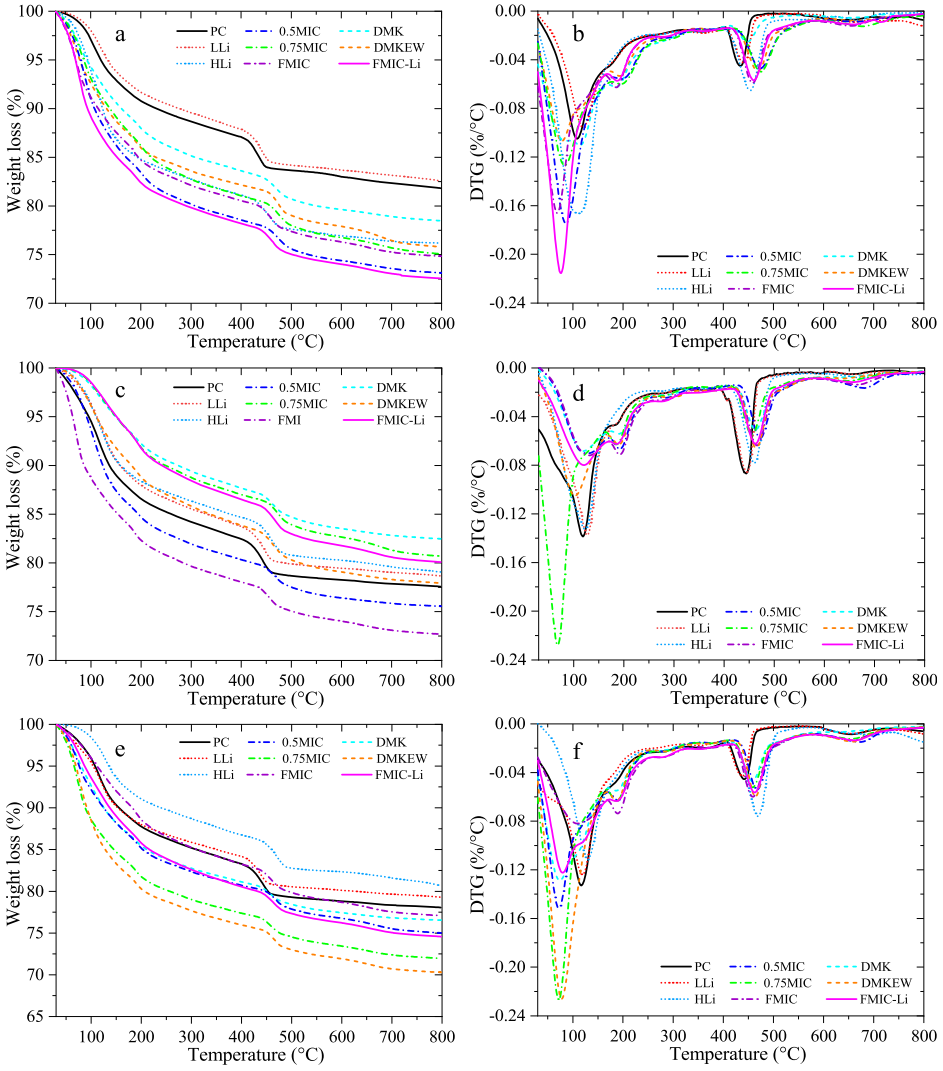

Fig. A.1. TGA and DTG curves of selected blends after (a, b) 7 days, (c, d) 14 days, and (e, f) 28 days of hydration: (a, c, e) relative weight loss; (b, d, f) derivative of weight loss.

References

[1] R. Guo, J. Wang, L. Bing, D. Tong, P. Ciais, S.J. Davis, R.M. Andrew, F. Xi, Z. Liu, Global CO 2 uptake by cement from 1930 to 2019, Earth Syst. Sci. Data 13 (4) (2021) 1791–1805, https://doi.org/10.5194/essd-13-1791-2021.

[2] Csa-A23, 1, Concrete Materials and Methods of Concrete Construction , Appendix B,Alkali-Aggregate Reaction, Canadian Standards Association, Toronto, Canada, 2004.

[3] X. Feng, M. Thomas, T. Bremner, K.J. Folliard, B. Fournier, New observations on the mechanism of lithium nitrate against alkali silica reaction (ASR), Cement Concr. Res. 40 (1) (2010) 94–101, https://doi.org/10.1016/j.cemconres.2009.07.017.

[4] M. Kawamura, H. Fuwa, Effects of lithium salts on ASR gel composition and expansion of mortars, Cement Concr. Res. 33 (6) (2003) 913–919, https://doi.org/10.1016/S0008-8846(02)01092-X.

[5] S.M. Shafaatian, A. Akhavan, H. Maraghechi, F. Rajabipour, How does fly ash mitigate alkali–silica reaction (ASR) in accelerated mortar bar test (ASTM C1567)? Cem. Concr. Compos. 37 (2013) 143–153, https://doi.org/10.1016/j.cemconcomp.2012.11.004.

[6] A. Brykov, A. Anisimova, N. Rozenkova, M. Hadi, M. Mokeev, The impact of aluminum-and iron-bearing admixtures on the resistance of portland cement mortars to alkali-silica reaction and sulfate attack, Mater. Sci. Appl. 6 (6) (2015) 539.

[7] M. Antoni, J. Rossen, F. Martirena, K. Scrivener, Cement substitution by a combination of metakaolin and limestone, Cement Concr. Res. 42 (12) (2012) 1579–1589, https://doi.org/10.1016/j.cemconres.2012.09.006.

[8] C. Tremblay, M.-A. Bérubé, B. Fournier, M.D. Thomas, K.J. Folliard, Effectiveness of lithium-based products in concrete made with Canadian natural aggregates susceptible to alkali-silica reactivity, ACI Mater. J. 104 (2) (2007) 195.

[9] G. Ke, W. Li, R. Li, Y. Li, G. Wang, Mitigation effect of waste glass powders on alkali–silica reaction (ASR) expansion in cementitious composite, Intern. J. Concr. Struc. Mater. 12 (1) (2018) 1–14.

[10] B. Craeye, M. Geirnaert, G. De Schutter, Super absorbing polymers as an internal curing agent for mitigation of early-age cracking of high-performance concrete bridge decks, Construct. Build. Mater. 25 (1) (2011) 1–13, https://doi.org/10.1016/j.conbuildmat.2010.06.063.

[11] D.P. Bentz, O.M. Jensen, Mitigation strategies for autogenous shrinkage cracking, Cem. Concr. Compos. 26 (6) (2004) 677–685.

[12] X. Sun, B. Zhang, Q. Dai, X. Yu, Investigation of internal curing effects on microstructure and permeability of interface transition zones in cement mortar with SEM imaging, transport simulation and hydration modeling techniques, Construct. Build. Mater. 76 (2015) 366–379.

[13] S. Zhutovsky, K. Kovler, Effect of internal curing on durability-related properties of high performance concrete, Cement Concr. Res. 42 (1) (2012) 20–26.

[14] D.P. Bentz, W.J. Weiss, Internal Curing: a 2010 State-Of-The-Art Review, US Department of Commerce, National Institute of Standards and Technology, 2011.

[15] J. Justs, M. Wyrzykowski, D. Bajare, P. Lura, Internal curing by superabsorbent polymers in ultra-high performance concrete, Cement Concr. Res. 76 (2015) 82–90.

[16] F. Liu, J. Wang, X. Qian, J. Hollingsworth, Internal curing of high performance concrete using cenospheres, Cement Concr. Res. 95 (2017) 39–46.

[17] H. Kim, H.-K. Lee, Hydration kinetics of high-strength concrete with untreated coal bottom ash for internal curing, Cem. Concr. Compos. 91 (2018) 67–75.

[18] C. Rößler, D.-D. Bui, H.-M. Ludwig, Rice husk ash as both pozzolanic admixture and internal curing agent in ultra-high performance concrete, Cem. Concr. Compos. 53 (2014) 270–278.

[19] B. Akcay, M.A. Tasdemir, Effects of distribution of lightweight aggregates on internal curing of concrete, Cem. Concr. Compos. 32 (8) (2010) 611–616.

[20] B.J. Mohr, Durability of Pulp Fiber-Cement Composites, School of Civil and Environmental Engineering, Georgia Institute of Technology, 2005.

[21] S. Barbhuiya, P. Chow, S. Memon, Microstructure, hydration and nanomechanical properties of concrete containing metakaolin, Construct. Build. Mater. 95 (2015) 696–702.

[22] S. Wild, J.M. Khatib, A. Jones, Relative strength, pozzolanic activity and cement hydration in superplasticised metakaolin concrete, Cement Concr. Res. 26 (10) (1996) 1537–1544.

[23] J. Khatib, S. Wild, Pore size distribution of metakaolin paste, Cement Concr. Res. 26 (10) (1996) 1545–1553.

[24] K. Gruber, T. Ramlochan, A. Boddy, R. Hooton, M. Thomas, Increasing concrete durability with high-reactivity metakaolin, Cem. Concr. Compos. 23 (6) (2001) 479–484.

[25] L. Courard, A. Darimont, M. Schouterden, F. Ferauche, X. Willem, R. Degeimbre, Durability of mortars modified with metakaolin, Cement Concr. Res. 33 (9) (2003) 1473–1479.

[26] E.J. Sare, T.L. Adkins, Kaolins Having Controlled Water Absorption, Oil Absorption, or Porosity, 2006.

[27] F. Lagier, K.E. Kurtis, Influence of Portland cement composition on early age reactions with metakaolin, Cement Concr. Res. 37 (10) (2007) 1411–1417, https://doi.org/10.1016/j.cemconres.2007.07.002.

[28] J. Wei, B. Gencturk, Hydration of ternary Portland cement blends containing metakaolin and sodium bentonite, Cement Concr. Res. 123 (2019), 105772.

[29] D. Luo, A. Sinha, M. Adhikari, J. Wei, Mitigating alkali-silica reaction through metakaolin-based internal conditioning: new insights into property evolution and mitigation mechanism, Cement Concr. Res. 159 (2022), https://doi.org/10.1016/j.cemconres.2022.106888.

[30] D. Kulik, GEMS-PSI 2.1, PSI-Villigen, Switzerland, 2005.

[31] ASTMC150/C150M, Standard Specification for Portland Cement, 2021.

[32] ASTMD281-12, Standard Test Method for Oil Absorption of Pigments by Spatula Rub-Out, 2021.

[33] T. Kim, J. Olek, Effects of sample preparation and interpretation of thermogravimetric curves on calcium hydroxide in hydrated pastes and mortars, Transport. Res. Rec. 2290 (1) (2012) 10–18, https://doi.org/10.3141/2290-02.

[34] A. Dunster, J. Parsonage, M. Thomas, The pozzolanic reaction of metakaolinite and its effects on Portland cement hydration, J. Mater. Sci. 28 (5) (1993) 1345–1350.

[35] X. Wang, Analysis of hydration-mechanical-durability properties of metakaolin blended concrete, Appl. Sci. 7 (10) (2017) 1087.

[36] J.F. Young, W. Hansen, Volume Relationships for CSH Formation Based on Hydration Stoichiometries, vol. 85, MRS Online Proceedings Library Archive, 1986.

[37] X. Wang, H. Lee, Modeling the hydration of concrete incorporating fly ash or slag, Cement Concr. Res. 40 (7) (2010) 984–996.

[38] G. Le Saoût, V. Kocaba, K. Scrivener, Application of the Rietveld method to the analysis of anhydrous cement, Cement Concr. Res. 41 (2) (2011) 133–148, https://doi.org/10.1016/j.cemconres.2010.10.003.

[39] B.H. Toby, R factors in Rietveld analysis: how good is good enough? Powder Diffr. 21 (1) (2006) 67–70, https://doi.org/10.1154/1.2179804.

[40] A.L. Morris, M.W. MacArthur, E.G. Hutchinson, J.M. Thornton, Stereochemical quality of protein structure coordinates, Proteins: Struct., Funct., Bioinf. 12 (4) (1992) 345–364, https://doi.org/10.1002/prot.340120407.

[41] K.S. Sing, Adsorption methods for the characterization of porous materials, Adv. Colloid Interface Sci. 76 (1998) 3–11.

[42] M. Saeidpour, L. Wadsö, Moisture equilibrium of cement based materials containing slag or silica fume and exposed to repeated sorption cycles, Cement Concr. Res. 69 (2015) 88–95.

[43] K. Sing, D. Everett, R. Haul, L. Moscou, R. Pierotti, J. Rouquerol, Siemieniewska Pure Appl, Chem 57 (1985) 603.

[44] X. Tang, N. Ripepi, K.A. Valentine, C. Keles, T. Long, A. Gonciaruk, Water vapor sorption on Marcellus shale: measurement, modeling and thermodynamic analysis, Fuel 209 (2017) 606–614.

[45] G. Sang, S. Liu, D. Elsworth, Water vapor sorption properties of Illinois shales under dynamic water vapor conditions: experimentation and modeling, Water Resour. Res. 55 (8) (2019) 7212–7228.

[46] L. Malm, A.-S.K. Danielsson, A. Sand, J. Rosenkranz, I. Ymén, Application of Dynamic Vapor Sorption for evaluation of hydrophobicity in industrial-scale froth flotation, Miner. Eng. 127 (2018) 305–311.

[47] M. Thommes, K. Kaneko, A.V. Neimark, J.P. Olivier, F. Rodriguez-Reinoso, J. Rouquerol, K.S. Sing, Physisorption of gases, with special reference to the evaluation of surface area and pore size distribution (IUPAC Technical Report), Pure Appl. Chem. 87 (9–10) (2015) 1051–1069, https://doi.org/10.1515/pac-2014-1117.

[48] R.M. Espinosa, L. Franke, Inkbottle pore-method: prediction of hygroscopic water content in hardened cement paste at variable climatic conditions, Cement Concr. Res. 36 (10) (2006) 1954–1968, https://doi.org/10.1016/j.cemconres.2006.06.011.

[49] M.M. Costoya Fernández, Effect of Particle Size on the Hydration Kinetics and Microstructural Development of Tricalcium Silicate, EPFL, 2008.

[50] M. Millard, K. Kurtis, Effects of lithium nitrate admixture on early-age cement hydration, Cement Concr. Res. 38 (4) (2008) 500–510.

[51] B. Lothenbach, K. Scrivener, R. Hooton, Supplementary cementitious materials, Cement Concr. Res. 41 (12) (2011) 1244–1256.

[52] W. Li, M. Fall, Strength and self-desiccation of slag-cemented paste backfill at early ages: link to initial sulphate concentration, Cem. Concr. Compos. 89 (2018) 160–168.

[53] A. Noumowe, Effet de hautes températures (20-600 C) sur le béton: cas particulier du béton a hautes performances, INSA, Lyon, 1995.

[54] L. Pelletier-Chaignat, F. Winnefeld, B. Lothenbach, G. Le Saout, C.J. Müller, C. Famy, Influence of the calcium sulphate source on the hydration mechanism of Portland cement–calcium sulphoaluminate clinker–calcium sulphate binders, Cem. Concr. Compos. 33 (5) (2011) 551–561.

[55] D. Luo, J. Wei, Hydration kinetics and phase evolution of Portland cement composites containing sodium-montmorillonite functionalized with a Non-Ionic surfactant, Construct. Build. Mater. 333 (2022), 127386, https://doi.org/10.1016/j.conbuildmat.2022.127386.

[56] Y. Zhang, J. Chang, J. Ji, AH3 phase in the hydration product system of AFt-AFm-AH3 in calcium sulfoaluminate cements: a microstructural study, Construct. Build. Mater. 167 (2018) 587–596, https://doi.org/10.1016/j.conbuildmat.2018.02.052.

[57] D. Luo, J. Wei, Upgrading sodium montmorillonite into a reactive internal curing agent for sustainable cement composites through non-ionic functionalization, Compos. B Eng. 242 (21) (2022), 110076, https://doi.org/10.1016/j.compositesb.2022.110076.

[58] M.J. Millard, Effects of Lithium Nitrate Admixture on Early Age Concrete Behavior, Georgia Institute of Technology, 2006.

[59] F. Avet, X. Li, K. Scrivener, Determination of the amount of reacted metakaolin in calcined clay blends, Cement Concr. Res. 106 (2018) 40–48.

[60] K. Vance, M. Aguayo, T. Oey, G. Sant, N. Neithalath, Hydration and strength development in ternary portland cement blends containing limestone and fly ash or metakaolin, Cem. Concr. Compos. 39 (2013) 93–103.

[61] M. Gbozee, K. Zheng, F. He, X. Zeng, The influence of aluminum from metakaolin on chemical binding of chloride ions in hydrated cement pastes, Appl. Clay Sci. 158 (2018) 186–194.

[62] H.F. Taylor, Cement Chemistry, Thomas Telford London, 1997.
[63] H. Taylor, Nanostructure of C· S· H: current status, Adv. Cement Base Mater. 1 (1) (1993) 38–46, https://doi.org/10.1016/1065-7355(93)90006-A.
[64] Z. Yan-Rong, K. Xiang-Ming, L. Zi-Chen, L. Zhen-Bao, Z. Qing, D. Bi-Qin, X. Feng, Influence of triethanolamine on the hydration product of portlandite in cement paste and the mechanism, Cement Concr. Res. 87 (2016) 64–76, https://doi.org/10.1016/j.cemconres.2016.05.009.
[65] N. Meller, C. Hall, K. Kyritsis, G. Giriat, Synthesis of cement based CaO–Al2O3–SiO2–H2O (CASH) hydroceramics at 200 and 250 C: Ex-situ and in-situ diffraction, Cement Concr. Res. 37 (6) (2007) 823–833, https://doi.org/10.1016/j.cemconres.2007.03.006.
[66] N. Shanahan, A. Markandeya, A. Elnihum, Y.P. Stetsko, A. Zayed, Multi-technique investigation of metakaolin and slag blended Portland cement pastes, Appl. Clay Sci. 132 (2016) 449–459, https://doi.org/10.1016/j.clay.2016.07.015.
[67] S.A. Yaseen, G.A. Yiseen, Z. Li, Elucidation of calcite structure of calcium carbonate formation based on hydrated cement mixed with graphene oxide and reduced graphene oxide, ACS Omega 4 (6) (2019) 10160–10170.
[68] M. Mollah, W. Yu, R. Schennach, D.L. Cocke, A Fourier transform infrared spectroscopic investigation of the early hydration of Portland cement and the influence of sodium lignosulfonate, Cement Concr. Res. 30 (2) (2000) 267–273.
[69] L. Fernández-Carrasco, E. Vázquez, Reactions of fly ash with calcium aluminate cement and calcium sulphate, Fuel 88 (9) (2009) 1533–1538.
[70] I. García-Lodeiro, A. Fernández-Jiménez, M.T. Blanco, A. Palomo, FTIR study of the sol–gel synthesis of cementitious gels: C–S–H and N–A–S–H, J. Sol. Gel Sci. Technol. 45 (1) (2008) 63–72.
[71] E. Kapeluszna, Ł. Kotwica, A. Różycka, Ł. Gołek, Incorporation of Al in CASH gels with various Ca/Si and Al/Si ratio: microstructural and structural characteristics with DTA/TG, XRD, FTIR and TEM analysis, Construct. Build. Mater. 155 (2017) 643–653, https://doi.org/10.1016/j.conbuildmat.2017.08.091.
[72] S. Puligilla, P. Mondal, Co-existence of aluminosilicate and calcium silicate gel characterized through selective dissolution and FTIR spectral subtraction, Cement Concr. Res. 70 (2015) 39–49.
[73] S. Barbhuiya, S. Mukherjee, H. Nikraz, Effects of nano-Al2O3 on early-age microstructural properties of cement paste, Construct. Build. Mater. 52 (2014) 189–193.
[74] M. Repacholi, Clay Mineralogy: Spectroscopic and Chemical Determinative Methods, Springer Science & Business Media, 2012.
[75] X. Ben, L. Jiang, M.-Z. Guo, W. Jin, L. Chen, F. Zhi, S. Gao, K. Xia, Effect of lithium citrate on hydration of cement paste, J. Build. Eng. 52 (2022), 104425, https://doi.org/10.1016/j.jobe.2022.104425.
[76] C.C.D. Coumes, M. Dhoury, J.-B. Champenois, C. Mercier, D. Damidot, Combined effects of lithium and borate ions on the hydration of calcium sulfoaluminate cement, Cement Concr. Res. 97 (2017) 50–60, https://doi.org/10.1016/j.cemconres.2017.03.006.
[77] C.C.D. Coumes, M. Dhoury, J.-B. Champenois, C. Mercier, D. Damidot, Physico-chemical mechanisms involved in the acceleration of the hydration of calcium sulfoaluminate cement by lithium ions, Cement Concr. Res. 96 (2017) 42–51, https://doi.org/10.1016/j.cemconres.2017.03.004.
[78] A. Kunhi Mohamed, P. Moutzouri, P. Berruyer, B.J. Walder, J. Siramanont, M. Harris, M. Negroni, S.C. Galmarini, S.C. Parker, K.L. Scrivener, The atomic-level structure of cementitious calcium aluminate silicate hydrate, J. Am. Chem. Soc. 142 (25) (2020) 11060–11071, https://doi.org/10.1021/jacs.0c02988.
[79] J.R. Mercury, P. Pena, A. De Aza, X. Turrillas, I. Sobrados, J. Sanz, Solid-state 27Al and 29Si NMR investigations on Si-substituted hydrogarnets, Acta Mater. 55 (4) (2007) 1183–1191, https://doi.org/10.1016/j.actamat.2006.09.032.
[80] Z. Dai, T.T. Tran, J. Skibsted, Aluminum Incorporation in the C–S–H phase of white Portland cement–metakaolin blends studied by 27 Al and 29 Si MAS NMR spectroscopy, J. Am. Ceram. Soc. 97 (8) (2014) 2662–2671, https://doi.org/10.1111/jace.13006.
[81] B.Z. Dilnesa, B. Lothenbach, G. Renaudin, A. Wichser, D. Kulik, Synthesis and characterization of hydrogarnet Ca3 (AlxFe1−x) 2 (SiO4) y (OH) 4 (3− y), Cement Concr. Res. 59 (2014) 96–111.
[82] B. Lothenbach, D.A. Kulik, T. Matschei, M. Balonis, L. Baquerizo, B. Dilnesa, G. D. Miron, R.J. Myers, Cemdata18: a chemical thermodynamic database for hydrated Portland cements and alkali-activated materials, Cement Concr. Res. 115 (2019) 472–506.
[83] E. Freyburg, A. Berninger, Field experiences in concrete deterioration by thaumasite formation: possibilities and problems in thaumasite analysis, Cem. Concr. Compos. 25 (8) (2003) 1105–1110.
[84] D. Damidot, F. Glasser, Investigation of the CaO-Al2O3-SiO2-H2O system at 25 C by thermodynamic calculations, Cement Concr. Res. 25 (1) (1995) 22–28.
[85] P. De Silva, F.P. Glasser, Phase relations in the system CaO-Al2O3-SiO2-H2O relevant to metakaolin-calcium hydroxide hydration, Cement Concr. Res. 23 (3) (1993) 627–639.
[86] V. Rahhal, R. Talero, Very early age detection of ettringite from pozzolan origin, Construct. Build. Mater. 53 (2014) 674–679.
[87] K. Gijbels, Y. Pontikes, P. Samyn, S. Schreurs, W. Schroeyers, Effect of NaOH content on hydration, mineralogy, porosity and strength in alkali/sulfate-activated binders from ground granulated blast furnace slag and phosphogypsum, Cement Concr. Res. 132 (2020), 106054.
[88] W. Kunther, Z. Dai, J. Skibsted, Thermodynamic modeling of hydrated white Portland cement–metakaolin–limestone blends utilizing hydration kinetics from 29Si MAS NMR spectroscopy, Cement Concr. Res. 86 (2016) 29–41.
[89] K. Liu, M. Deng, L. Mo, J. Tang, Deterioration mechanism of Portland cement paste subjected to sodium sulfate attack, Adv. Cement Res. 27 (8) (2015) 477–486.
[90] B. Lothenbach, F. Winnefeld, Thermodynamic modelling of the hydration of Portland cement, Cement Concr. Res. 36 (2) (2006) 209–226.
[91] J. Tang, S. Wei, W. Li, S. Ma, P. Ji, X. Shen, Synergistic effect of metakaolin and limestone on the hydration properties of Portland cement, Construct. Build. Mater. 223 (2019) 177–184.
[92] F. Zunino, K. Scrivener, The reaction between metakaolin and limestone and its effect in porosity refinement and mechanical properties, Cem, Concr. Res. 140 (2020), 106307.
[93] E. Badogiannis, G. Kakali, G. Dimopoulou, E. Chaniotakis, S. Tsivilis, Metakaolin as a main cement constituent. Exploitation of poor Greek kaolins, Cem. Concr. Compos. 27 (2) (2005) 197–203.
[94] A. Vavričuk, V. Bokan-Bosiljkov, S. Kramar, The influence of metakaolin on the properties of natural hydraulic lime-based grouts for historic masonry repair, Construct. Build. Mater. 172 (2018) 706–716.
[95] J. Wei, C. Meyer, Sisal fiber-reinforced cement composite with Portland cement substitution by a combination of metakaolin and nanoclay, J. Mater. Sci. 49 (21) (2014) 7604–7619, https://doi.org/10.1007/s10853-014-8469-8.
[96] J.L. Provis, S.A. Bernal, Geopolymers and related alkali-activated materials 44 (2014) 299–327, https://doi.org/10.1146/annurev-matsci-070813-113515.
[97] A. Palomo, M.T. Blanco-Varela, M. Granizo, F. Puertas, T. Vazquez, M. Grutzeck, Chemical stability of cementitious materials based on metakaolin, Cement Concr. Res. 29 (7) (1999) 997–1004.
[98] S. Tang, X. Cai, Z. He, H. Shao, Z. Li, E. Chen, Hydration process of fly ash blended cement pastes by impedance measurement, Construct. Build. Mater. 113 (2016) 939–950.
[99] R. Fernández, M. Rodríguez, R.V. de la Villa, J. Cuevas, Geochemical constraints on the stability of zeolites and C–S–H in the high pH reaction of bentonite, Geochem. Cosmochim. Acta 74 (3) (2010) 890–906.
[100] C. Shi, A. Fernández-Jiménez, Stabilization/solidification of hazardous and radioactive wastes with alkali-activated cements, J. Hazard Mater. 137 (3) (2006) 1656–1663.
[101] E. Prud'Homme, P. Michaud, E. Joussein, S. Rossignol, Influence of raw materials and potassium and silicon concentrations on the formation of a zeolite phase in a geopolymer network during thermal treatment, J. Non-Cryst. Solids 358 (16) (2012) 1908–1916.
[102] H.R. Khalid, N. Lee, I. Choudhry, Z. Wang, H.-K. Lee, Evolution of zeolite crystals in geopolymer-supported zeolites: effects of composition of starting materials, Mater. Lett. 239 (2019) 33–36.
[103] C.S. Cundy, P.A. Cox, The hydrothermal synthesis of zeolites: precursors, intermediates and reaction mechanism, Microporous Mesoporous Mater. 82 (1–2) (2005) 1–78.
[104] F. Pacheco-Torgal, J. Castro-Gomes, S. Jalali, Alkali-activated binders: a review: Part 1. Historical background, terminology, reaction mechanisms and hydration products, Construct. Build. Mater. 22 (7) (2008) 1305–1314.
[105] S. Monkman, Y. Sargam, L. Raki, Comparing the effects of in-situ nano-calcite development and ex-situ nano-calcite addition on cement hydration, Construct. Build. Mater. 321 (2022), 126369, https://doi.org/10.1016/j.conbuildmat.2022.126369.
[106] G. Ovcharenko, E. Ibe, A. Sandrasheva, A. Viktorov, Contact Strength of CSH Cement Phase, E3S Web of Conferences, EDP Sciences, 2019, 02031.
[107] Y. Yi, X. Zheng, S. Liu, A. Al-Tabbaa, Comparison of reactive magnesia-and carbide slag-activated ground granulated blastfurnace slag and Portland cement for stabilisation of a natural soil, Appl. Clay Sci. 111 (2015) 21–26.
[108] P.S. de Silva, F.P. Glasser, Phase relations in the system CaO·Al2O3·SiO2·H2O relevant to metakaolin - calcium hydroxide hydration, Cement Concr. Res. 23 (3) (1993) 627–639, https://doi.org/10.1016/0008-8846(93)90014-Z.
[109] B.Z. Dilnesa, B. Lothenbach, G. Renaudin, A. Wichser, D. Kulik, Synthesis and characterization of hydrogarnet Ca3(AlxFe1−x)2(SiO4)y(OH)4(3−y), Cement Concr. Res. 59 (2014) 96–111, https://doi.org/10.1016/j.cemconres.2014.02.001.
[110] S. Martínez-Ramírez, M. Frias, Micro-Raman study of stable and metastable phases in metakaolin/Ca (OH) 2 system cured at 60° C, Appl. Clay Sci. 51 (3) (2011) 283–286, https://doi.org/10.1016/j.clay.2010.12.001.
[111] D. Torréns-Martín, L. Fernández-Carrasco, S. Martínez-Ramírez, J. Ibáñez, L. Artús, T. Matschei, Raman spectroscopy of anhydrous and hydrated calcium aluminates and sulfoaluminates, J. Am. Ceram. Soc. 96 (11) (2013) 3589–3595, https://doi.org/10.1111/jace.12535.
[112] D. Luo, J. Wei, Understanding the role of a novel internal conditioning technique with functionalized montmorillonite in cement hydration kinetics, Construct. Build. Mater. 385 (2023), 131223, https://doi.org/10.1016/j.conbuildmat.2023.131223.
[113] F.P. Glasser, A. Kindness, S.A. Stronach, Stability and solubility relationships in AFm phases: Part I. Chloride, sulfate and hydroxide, Cement Concr. Res. 29 (6) (1999) 861–866, https://doi.org/10.1016/S0008-8846(99)00055-1.
[114] J. MacDowell, T. Huang, A. Chowdhury, Evaluation of Stratlingite-Hydrogarnet Glass Cement as a Quick-Setting Patching Material, Strategic Highway Research Program, National Research Council, Washington, DC, United States, 1992.
[115] T. Matschei, B. Lothenbach, F.P. Glasser, Thermodynamic properties of portland cement hydrates in the system CaO–Al2O3–SiO2–CaSO4–CaCO3–H2O, Cement Concr. Res. 37 (10) (2007) 1379–1410, https://doi.org/10.1016/j.cemconres.2007.06.002.
[116] K.A. Snyder, Mineralogical and Microstructural Evolution in Hydrating Cementitious Systems, CBP-TR-2009-002-C2, Rev. 0, National Institute of Standards and Technology, 2009.
[117] R. Xiao, X. Jiang, M. Zhang, P. Polaczyk, B. Huang, Analytical investigation of phase assemblages of alkali-activated materials in CaO-SiO2-Al2O3 systems: the

management of reaction products and designing of precursors, Mater. Des. 194 (2020), 108975, https://doi.org/10.1016/j.matdes.2020.108975.

[118] R. Taylor, I.G. Richardson, R.M.D. Brydson, Composition and microstructure of 20-year-old ordinary Portland cement–ground granulated blast-furnace slag blends containing 0 to 100% slag, Cement Concr. Res. 40 (7) (2010) 971–983, https://doi.org/10.1016/j.cemconres.2010.02.012.

[119] B. Lothenbach, D. Rentsch, E. Wieland, Hydration of a silica fume blended low-alkali shotcrete cement, Phys. Chem. Earth 70–71 (2014) 3–16, https://doi.org/10.1016/j.pce.2013.09.007. Parts A/B/C.